

ABSTRACT

Title of Thesis COMPUTATIONAL STUDIES ON DROPLET
DYNAMICS AT INTERSECTING FLOWS IN
MICROFLUIDIC JUNCTIONS

Sai Kishore Mamidi, Master of Science, 2010

Thesis directed by: Professor Panagiotis Dimitrakopoulos
Department of Chemical and Biomolecular Engineering

The current thesis involves a computational study of drop dynamics in microfluidic junctions, at the moderate capillary number of $Ca = 0.1$. We utilize a three-dimensional Spectral Boundary Element algorithm to determine the drop motion in the presence of intersecting lateral flows in microfluidic T-junctions and cross-junctions, and analyze the effect on drop deformation and motion with varying shear rates in the channels leading to the junctions, and for two different viscosity ratios ($\lambda = 0.2, 20.0$) between the drop and the surrounding fluid.

We find that the presence of intersecting flows, drastically affects the transient behavior at the junctions, and the drop reaches steady state further away, both upstream and downstream of these junctions. The time taken to reach steady state in the T-junctions was found to be significantly greater than that in the cross-junction, under identical conditions. Drop velocities were found to be a linear function of the effective shear rate in the channel, and length scale fluctuations as high as 30% were observed in the junction region for the cases studied in the thesis.

We observed that the excess pressure drop with respect to the flow of a single phase fluid was strongly related to the length of the droplet at a given spatial coordinate. The peak surface area of the drop in the junction was found to be a slightly non-linear function of the flow rates in the lateral channels, and almost all the surface area increase was occurring at the head of the drop, in the direction of the flow. Velocity was found to be a weak, inverse function of the viscosity ratio, the increase in drop surface area was found to be greater in drops with lower viscosity. It was found that the junction bend radius/smoothness had a more significant effect on the dynamics of the drop in a T-junction, compared to that in a cross-junction.

COMPUTATIONAL STUDIES ON DROPLET DYNAMICS AT
INTERSECTING FLOWS IN MICROFLUIDIC JUNCTIONS

by

Sai Kishore Reddy Mamidi

Thesis submitted to the Faculty of the Graduate School of the
University of Maryland, College Park in partial fulfillment
of the requirements for the degree of
Master of Science
2010

Advisory Committee:

Professor Panagiotis Dimitrakopoulos, Chair/Advisor

Professor Michail Anisimov

Professor Srinivasa R. Raghavan

Professor Jeffery Klauda

© Copyright by
Sai Kishore Reddy Mamidi
2010

Acknowledgments

I owe my gratitude to all the people who have made this thesis possible and because of whom my graduate experience has been one that I will cherish forever. First and foremost I'd like to thank my advisor, Professor Panagiotis Dimitrakopoulos for giving me an invaluable opportunity to work on challenging and interesting projects. It has been a great learning experience to work with him, and want to thank him for patiently correcting me whenever I have been wrong.

Special thanks to my colleagues at the Bio Fluid Dynamics Laboratory - Shugi Kuriakose and Moon Soo Lee, for their invaluable help, enriching discussions, and most importantly for bearing my periodic tantrums. It was really a blessing to have had such caring lab mates.

I owe my deepest thanks to my family - my mother, father, late grandmother, loving sisters Ranjitha and Nanditha, and their sweetest little kids Pooja, Teja and Nitya. I thank them for standing by me and guiding me through both the good, and the adverse times. Words cannot express the gratitude I owe them.

I would like to acknowledge the moral support from Mr. John Shackford, at ThreeECompany. The faith he has shown in me over the past year has inspired me more than anything I can think of. Also a special note of thanks to my dear friend Susmitha Tadishetty for the support and motivation over the past couple of years. I also owe my sincere gratitude to many others, whom I have not specifically mentioned, and want to say that this thesis was possible only because of the immense support from all my family and friends.

This research was supported in part by the Petroleum Research Fund of the American Chemical Society, and the National Center for Supercomputing Applications in Illinois.

Table of Contents

List of Figures	v
List of Abbreviations	viii
1 Introduction	1
1.1 Relevance of the Topic	1
1.1.1 Fluid flow in Microchannels	3
1.1.2 Shape as a Critical Parameter	5
1.2 Literature Survey	6
1.2.1 Droplet Deformation and Pressure Drop	7
1.2.2 Studies on drop dynamics in Microfluidic Junctions	10
1.3 Summary and Layout of Present Thesis	14
2 Mathematical Formulation	16
2.1 From Stokes equations to Boundary Integral equations	16
2.2 BIE for a free suspended drop	18
2.3 BIE for a drop in a confined domain	19
2.4 Spectral element formulation	21
2.5 Problem parameters and dimensionless analysis	22
2.6 Boundary Conditions	24
3 Results and Discussion	27
3.1 Microfluidic Cross-Junctions	28
3.1.1 Cross-Junctions with 90° bends (bend radius $r_b = 0$)	28
3.1.2 Cross-Junctions with non-zero bend radius ($r_b > 0$)	38
3.2 Microfluidic T-junctions	47
3.2.1 T-junctions with 90° bends (bend radius $r_b = 0$)	47
3.3 Conclusions	59
Bibliography	61

List of Figures

2.1	Illustrations for the geometry of the BIEs (2.3) and (2.6).	17
2.2	Illustration of a droplet freely suspended in an infinite fluid.	19
2.3	Illustration of drop suspended in the fluid inside a rectangular channel.	20
2.4	2D illustration for the cross-junction geometry.	23
2.5	Coordinates for a rectangular cross-section, flow symmetric with respect to both y and z axis	25
2.6	Velocity boundary conditions for square cross-sections of length 2, as applied at the fluid boundaries, for flow along increasing- x direction.	26
3.1	Representative geometry for a cross-junction with bend radius $r_b = 0$	30
3.2	Drop displacement along x -axis as a function of time t , in a microfluidic cross-junction, with bend radius $r_b = 0$ and $r_b = 2$, square cross-sectional length $b = 2$, shear rate along x -axis $X_{sh} = 1.0$, shear rate $Y_{sh} = 0.5$ along y -axis, capillary number $Ca = 0.1$ and viscosity ratio $\lambda = 0.2$	31
3.3	Drop velocity along x -axis U_x as a function of drop centroid x_c , in microfluidic cross-junctions with bend radius $r_b = 0$, square cross-sectional length $b = 2$, shear rate along x -axis $X_{sh} = 1.0$, varying shear rate Y_{sh} along y -axis, capillary number $Ca = 0.1$ and viscosity ratio $\lambda = 0.2$	32
3.4	Maximum droplet length (L_x, L_y, L_z), along x, y, z -axes respectively, and surface area as a function of drop centroid x_c , in a microfluidic cross-junction, with bend radius $r_b = 0$, square cross-sectional length $b = 2$, shear rate along x -axis $X_{sh} = 1.0$, varying shear rate Y_{sh} along y -axis, capillary number $Ca = 0.1$ and viscosity ratio $\lambda = 0.2$	33
3.5	Drop velocity along x -axis U_x as a function of drop centroid x_c , for viscosity ratio's $\lambda = 0.2, 20.0$, in a microfluidic cross-junction, with bend radius $r_b = 0$, square cross-sectional length $b = 2$, shear rate along x -axis $X_{sh} = 1.0$, shear rate along y -axis $Y_{sh} = 0.5$, capillary number $Ca = 0.1$	35
3.6	Maximum droplet length (L_x, L_y, L_z), along x, y, z -axes respectively, as a function of drop centroid x_c , for viscosity ratio $\lambda = 0.2$ and $\lambda = 20.0$, in a microfluidic cross-junction, with bend radius $r_b = 0$, square cross-sectional length $b = 2$, shear rate along x -axis $X_{sh} = 1.0$, shear rate along y -axis $Y_{sh} = 0.5$, capillary number $Ca = 0.1$	36
3.7	(a) Drop surface area as a function of drop centroid x_c , for viscosity ratio $\lambda = 0.2$ and $\lambda = 20.0$ (b) Excess pressure drop as a function of drop centroid x_c , for viscosity ratios $\lambda = 0.2$ and $\lambda = 20.0$ and (c) Droplet head and tail length along x -axis as a function of drop centroid x_c for viscosity ratio $\lambda = 20.0$, in a microfluidic cross-junction, with bend radius $r_b = 0$, square cross-sectional length $b = 2$, shear rate along x -axis $X_{sh} = 1.0$, shear rate along y -axis $Y_{sh} = 0.5$, capillary number $Ca = 0.1$	37

3.8	Illustration of geometry for a cross-junction with bend radius $r_b = 2$.	39
3.9	Drop velocity, U_x along x -axis, as a function of position x_c , in a microfluidic cross-junction, with bend radius $r_b = 2$, square cross-sectional length $b = 2$, shear rate along x -axis $X_{sh} = 1.0$, varying shear rate Y_{sh} along y -axis, capillary number $Ca = 0.1$ and viscosity ratio $\lambda = 0.2$.	40
3.10	Maximum droplet length (L_x, L_y, L_z) , along x, y, z -axes respectively, as a function of drop centroid x_c , in a microfluidic cross-junction, with bend radius $r_b = 2$, square cross-sectional length $b = 2$, shear rate along x -axis $X_{sh} = 1.0$, varying shear rate Y_{sh} along y -axis, capillary number $Ca = 0.1$ and viscosity ratio $\lambda = 0.2$.	41
3.11	(a) Drop surface area (b) Droplet head and tail length along x -axis (c) Droplet head and tail length along x -axis as a function of drop centroid x_c , for shear rate along y , $Y_{sh} = 0$, in a microfluidic cross-junction, with bend radius $r_b = 2$, square cross-sectional length $b = 2$, shear rate along x -axis $X_{sh} = 1.0$, capillary number $Ca = 0.1$ and viscosity ratio $\lambda = 0.2$.	42
3.12	Drop velocity U_x along x -axis, maximum drop length (L_x, L_y, L_z) as a function of drop centroid x_c , in microfluidic cross-junctions, with bend radius $r_b = 0$, and $r_b = 2$, square cross-sectional length $b = 2$, shear rate along x -axis $X_{sh} = 1.0$, shear rate along y -axis $Y_{sh} = 0.5$, capillary number $Ca = 0.1$ and viscosity ratio $\lambda = 0.2$.	43
3.13	(a) Drop surface area as a function of drop centroid x_c , and (b) Excess pressure drop in microfluidic cross-junction, with bend radius $r_b = 0$, and $r_b = 2$, square cross-sectional length $b = 2$, shear rate along x -axis $X_{sh} = 1.0$, shear rate along y -axis $Y_{sh} = 0.5$, capillary number $Ca = 0.1$ and viscosity ratio $\lambda = 0.2$.	44
3.14	Shape evolution of droplet in a microfluidic cross-junction, with bend radius $r_b = 2$, square cross-sectional length $b = 2$, shear rate along x -axis $X_{sh} = 1.0$, shear rate along y -axis $Y_{sh} = 0.5$, capillary number $Ca = 0.1$ and viscosity ratio $\lambda = 20.0$.	46
3.15	Illustration of geometry for a T-junction with bend radius $r_b = 0$.	48
3.16	Drop displacement along x, y -axes as a function of time t , in a microfluidic T-junction, with bend radius $r_b = 0$, square cross-sectional length $b = 2$, shear rate along x -axis $X_{sh} = 1.0$, shear rate $Y_{sh} = 0.5$ along y -axis, capillary number $Ca = 0.1$ and viscosity ratio $\lambda = 0.2$.	49
3.17	(a) Drop velocity along x -axis U_x (b) Drop velocity along y -axis U_y (c) Lateral drop displacement with respect to drop position x_c , in a microfluidic T-junction with bend radius $r_b = 0$, square cross-section of length $b = 2$, shear rate along x -axis $X_{sh} = 1.0$, shear rate along y -axis $Y_{sh} = 0.5$ capillary number $Ca = 0.1$ and viscosity ratio $\lambda = 0.2$.	51

3.18	(a) Maximum droplet length, along x , y and z -axes, (b) Droplet surface area as a function of drop centroid x_c , and (c) Excess pressure drop as a function of drop centroid x_c , in a microfluidic T-junction, with bend radius $r_b = 0$, square cross-section of length $b = 2$, shear rate along x -axis $X_{sh} = 1.0$, varying shear rate along y -axis $Y_{sh} = 0, 0.001, 0.1, 0.5$, capillary number $Ca = 0.1$ and viscosity ratio $\lambda = 0.2$.	52
3.19	(a) Drop velocity U_x along x -axis, (b) Drop velocity U_y along y -axis, (c) Lateral drop displacement (along y -axis) as a function of drop centroid x_c , in microfluidic T-junction, with bend radius $r_b = 0$, and $r_b = 2$, square cross-sectional length $b = 2$, shear rate along x -axis $X_{sh} = 1.0$, shear rate along y -axis $Y_{sh} = 0.5$, capillary number $Ca = 0.1$ and viscosity ratio $\lambda = 0.2$.	54
3.20	Drop length L_x, L_y, L_z along x, y, z -axes respectively and drop surface area as a function of drop centroid x_c in a microfluidic T-junction, with bend radius $r_b = 0$, and $r_b = 2$, square cross-sectional length $b = 2$, shear rate along x -axis $X_{sh} = 1.0$, shear rate along y -axis $Y_{sh} = 0.5$, capillary number $Ca = 0.1$ and viscosity ratio $\lambda = 0.2$.	55
3.21	Shape evolution of droplet in a microfluidic T-junction, with bend radius $r_b = 0$, square cross-section of length $b = 2$, shear rate along x -axis $X_{sh} = 1.0$, shear rate along y -axis $Y_{sh} = 0.5$, capillary number $Ca = 0.1$ and viscosity ratio $\lambda = 0.2$.	58

List of Abbreviations

Ca	Capillary number
Re	Reynolds number
$\lambda\mu$	Droplet viscosity
μ	Viscosity of ambient fluid
ρ_1	Droplet density
ρ_2	Density of ambient fluid
γ	Surface tension of drop interface
$\boldsymbol{\sigma}$	Stress tensor
p	Pressure
\mathbf{u}	Velocity
\mathbf{u}^∞	Undisturbed velocity
L_x	Maximum droplet length along x -axis
L_y	Maximum droplet length along y -axis
L_z	Maximum droplet length along z -axis
x_c	x -coordinate of drop centroid
y_c	y -coordinate of drop centroid
X_{sh}	Shear rate along the x -axis
Y_{sh}	Shear rate along the y -axis
ΔP^+	Excess pressure drop
U_x	Drop velocity along x -axis
U_y	Drop velocity along y -axis
RCJ	Right angled cross-junction
SCJ	Smooth cross-junction
RTJ	Right angled T-junction
STJ	Smooth T-Junction

Chapter 1

Introduction

The current thesis considers the problem of multiphase droplet dynamics in microfluidic junctions. We study the physical problem of Stokes flow in microfluidic T-junctions and cross-junctions and present a comparison with a straight square micro-channel, highlighting the change in dynamics, including the droplet velocities, drop surface areas, pressure drop etc., that occur because of the presence of intersecting flows.

1.1 Relevance of the Topic

It is not surprising that drops have been studied for more than a century now given that they control a diverse majority of natural, biological and industrial processes ranging from traditional usages like direct contact heat/mass exchangers [32], controlled polymer microstructures [11], to novel blood oxygenation or drug delivery methods [6]. There have been extensive experimental, theoretical and computational studies on soft particles (droplets, bubbles, capsules, vesicles etc.), which can be broadly classified into those involving droplet-deformation, bursting, coalescence, formation or particle adherence to solid and flexible boundaries. Each of these studies, apart from providing increased understanding of the fundamental underlying physics, are also merited for their specific real life engineering applications.

The study of droplet dynamics and deformation in confined microfluidic junctions is motivated by numerous applications in engineering and scientific applications, especially in microfluidic devices designed for *in situ* bio-assays, polymer electrolyte membrane fuel cells [48], MEMS, drug delivery, enhanced oil recovery and coating processes. Soft particles passing through intersecting flows, are also widely found in animal physiology, where, for instance, the blood cells pass through numerous constricted and intersecting flows. Understanding how the pressure drop along a channel depends on the length of the drops that move through it is crucial to designing valveless microfluidic networks, that route these bubbles from one region of the device to the next [29]. Understanding how bubbles/drops affect the flow resistance in microchannels is, a concern of determining the pumping or energy requirement for portable microfluidic devices involving two-phase flows, such as in a micro-direct methanol fuel cell [15].

The use of droplets as microreactors offers many advantages in comparison with single-phase microfluidics, such as confinement of reactants or prevention of longitudinal dispersion and cross contamination between subsequent samples. Additional benefits include reduction of unwanted adhesion/adsorption of the material confined in droplets at the channel walls and facilitated heat/mass transport due to enhanced internal mixing [34]. Microdroplets also allow the possibility of varying, in each droplet, the physicochemical conditions under which chemical or biochemical processes develop, opening the way to screening, and the fast mixing that takes place in each droplet [33].

Also, cells are biological units that can be viewed as droplet-like sensors and

actuators that detect and react to small chemical changes [53], and microfluidics can help develop *in situ* point of care medical devices, and other miniaturized bio-assay devices, provide better control over formation of emulsions [45], design efficient mixing devices, model novel drug delivery systems [6], DNA multi-plexing devices [42], and improve the efficiency of filtration devices for analyzing individual biological cells [70], a technology, which can potentially help detect the presence of diseases [70].

In conclusion, we can say that in order to realize all these prospects requires the control of elementary operations and a better understanding of the dynamics of the drops in complicated microchannels.

1.1.1 Fluid flow in Microchannels

Apart from requiring novel manufacturing methods, there are some fundamental differences between fluid flow in macro and micro geometries [50], and prominent among the differences is the absence of turbulence. On the macro scale, Newtonian fluids mix convectively, wherein inertia is often more important than viscosity. At the micro scale however, when two Newtonian fluid streams come together, they usually flow in parallel, without forming any eddies or turbulence, and the only mixing that occurs is the result of diffusion of molecules occurring across the fluids interface [49]. This is known as laminar flow, and if mixing is required in these micro-devices, it requires the development of special components to achieve it. Janasek *et al.* [31], describe in detail, the scaling relationships, that compare the macroscopic

and microscopic fluidic systems.

The fundamental difference in the physics of fluids flowing in microchannels, offers some significant advantages over their macro-level counterparts. One particularly useful characteristic of fluid flow in microsystems is electro-osmotic flow (EOF), which minimizes the broadening of plugs of sample that occurs with many pressure-driven systems, and allows very high resolution separations of ionic species [3]. EOF is a key contributor to electrophoretic separations of DNA in microchannels. Manipulation of multi-phase flows is another strength of microfluidic systems, which enables generation and manipulation of mono-disperse bubbles or droplets of a dispersed gas or liquid phase, in continuous liquid streams. Drops can also serve as compartments, which can allow the study of fast chemical reactions. Microfluidic devices are fast emerging as useful tools for biologists and chemists, allowing precise control of variables such as fluid shear rate, solute concentration [63] and inherent high throughput way of operation [17]. Beebe *et al.* [63] have shown that microchannels can be as much as 10 times more precise than the standard wells, used currently in drug screening. Another potentially useful characteristic of flow at this scale is their ability to manipulate fluids in channels with dimensions of the order of Debye layer [3].

Microfluidic devices find uses in important areas including analytical chemistry, chemical synthesis, cell biology, molecular biology, drug discovery, genomics, proteomics, diagnostics, environmental monitoring and national security [8]. As of today, the most highly developed of microfluidic applications, is probably in screening conditions (such as pH, ionic strength and composition, cosolvents, and con-

centrations), for protein crystallization. Microfluidics offer the potential to screen large number of conditions, to separate nucleation and growth of crystals, and to minimize the damage to crystals by handling once they have formed [64] other applications include separations coupled to mass-spectroscopy [27], high throughput screening in drug development, bio-analysis, single-cell examination [28]. Fluids in microchannels form the basis of new optical systems, a range of systems from waveguides comprising a liquid with a high index of refraction flowing laminarly between two streams of low-index cladding, to applications of fluids in lenses and Bragg mirrors [64].

1.1.2 Shape as a Critical Parameter

Drops are typically realized through intersecting, multi-phase fluid geometries [13], where the shape of microparticles is a critical parameter, as it affects the homogeneity of the resulting emulsions, and understanding drop dynamics in multi-phase systems will help us design devices to generate a targeted shapes.

Transport of particles in the biological systems, are affected by their shape. For instance, solid spherical particles must be less than 200 *nm* in diameter to successfully clear the non-symmetrical filtering units in spleen, but disk-shaped, flexible red blood cells with diameters of $\sim 8 \mu m$ routinely pass through the spleen [7]. In drug delivery, shape of particles, which directly affects the total surface area available, and the local curvature influence the targeting, adsorption, internalization capabilities of the drug [6]. A well known fact in pharmaceutical industry is that,

when conventional therapeutic drugs are encapsulated in polymer particles, they offer various advantages, including controlled release, protection from metabolism and degradation, and better targeting capabilities. Recent studies have established that shape induced inhibition of phagocytosis of drug delivery particles is possible, by minimizing the size normalized curvature of particles [6, 7, 38, 47].

To conclude, we can say that, just as size affects particle velocity, shape will affect diffusion and adhesion to walls in blood vessels, airways and intestines, albeit in more complex ways. Shape depends on the flow properties of particles, especially capillary number, viscosity ratio, orientation, symmetry, and proximity to vessel walls and such dependencies must be better understood.

1.2 Literature Survey

The current thesis builds directly on the theory and algorithms developed by Dimitrakopoulos *et al.* [61, 20, 21, 51], and the problems analyzed depend on, two main dimensionless parameters: (a) the ratio of the viscosity of the fluid inside the drop to that of the external fluid λ , and (b) the capillary number $Ca = \mu U / \gamma$, where μ is the viscosity of the external fluid, U is the average fluid velocity in a straight channel in the absence of a drop, and γ is the interfacial surface tension. In our study, we start with an initially spherical droplet, with radius, $a = 0.7$.

The following section presents some of the key historical milestones and studies that have lead to present day understanding of the topic of droplet dynamics.

1.2.1 Droplet Deformation and Pressure Drop

Studies investigating the characteristics of immersed objects began with Archimedes, when he determined the hydrostatic forces acting on an immersed object of any shape and density and formulated the concept of integrals that make possible such calculations [37]. But it was not until early 19th century, that researchers started exploring the dynamics of immersed deformable/soft objects like drops, capsules etc. and proved that drops of one fluid when placed in a second, shearing fluid, will deform [45]. Ever since then, one of the principal goals of experimental and numerical studies in this field has been to quantize the relevant parameters like deformation, shape, pressure-drop breakup etc. with respect to the available control parameters like the applied external shear, capillary number and viscosity ratio.

Taylor [54, 55] developed a first-order theoretical model and perform experimental analysis on the deformation and orientation of droplets in shearing flows, and soon after, Kopac and Chambers [5] performed a study of multiphase liquid-liquid droplets. Torza and Mason presented a thorough theoretical analysis of static two-phase drop configurations in 1970. Barthes-Biesel and Acrivos [2] developed a good theoretical model for predicting the droplet deformation and breakup.

Though Taylor's model [55] found good agreement with experimental results for small deformations, it failed at larger deformations, for which he later developed a slender-body theory [56]. Since then, numerous, more sophisticated numerical methodologies have been developed and employed for the study of deforming droplets. Youngren and Acrivos [69, 68] were the first to develop and apply the

Boundary Integral method for interfacial problems in Stokes regime, and determined the equilibrium shape of a droplet for $\lambda = 0$ in an axis-symmetric extensional flow. Rallison *et al.* [46, 44] calculated deformations for $\lambda > 0$, in extensional flows, and $\lambda = 1$ for non-axisymmetric shear flows.

Two-dimensional droplet models included by Navot [39], were initially based on an equi-distant partition of the interfacial curve, and the later models adopted cubic splines to represent the interfacial curve. Buckmaster and Flaherty [4] studied a deforming two-dimensional droplet for $\lambda = 1$. Dimitrakopoulos and Wang [58, 61] numerically implemented the three-dimensional model of droplet deformation. They studied the droplet dynamics in the case of straight square channels, and tubes, establishing the effect of varying λ and Ca . They also implemented a novel high-order/high-accuracy three-dimensional Spectral Boundary Element algorithm to the interfacial problem of viscous flow over a protuberance on the inner wall of a solid microtube. Dimitrakopoulos and Wang [61, 58, 59]. An additional numerical study of droplet deformations includes that of Shirani and Masoomi [48], who numerically simulated the deformation of a water droplet, adhering to a channel.

Fuerstman *et al.* [29] developed an experimental method to determine the effect of the bubbles, on the pressure drop between two points in a microchannel of rectangular cross-section, for capillary number Ca of the order of 10^{-3} , Reynolds number Re between 0.1 to 1. They conclude that the pressure drop is determined by the total number of bubbles present as well as the total length of the bubbles. Gupta *et al.* [35] studied the motion of air bubbles, flowing in square micro-channels, under the influence of gravity. The steady-state shapes and velocities of the bub-

bles as a function of the bubble size are determined experimentally, for varying bond, capillary, and Reynolds numbers. Cubaud and Mason [16] experimentally analyze the formation and evolution of threads and containing more viscous liquids surrounded by less viscous, immiscible liquids through hydrodynamic focusing in square microchannels

Cubaud and Ho [15] produced a steady and homogeneous flows of monodisperse bubbles and examined the two-phase flow maps and transition lines between flow regimes. They measure the bubble velocity, slip ratio between liquid and gas, two-phase flow pressure drop is measured and compared with single liquid flow pressure drop. Vanapalli *et al.* [57] experimentally study the effect of drop size, viscosity, and capillary number on the hydrodynamic resistance, for drops flowing in rectangular channels, for capillary numbers ranging from $0.001 \leq Ca \leq 0.01$. They conclude that for small drops (drop length/channel width $\sim < 4$), pressure drop is independent of the drop size and capillary number and weakly dependent on the viscosity ratio. Mudawar *et al.* [43] performed experimental and computational studies on adiabatic single phase flow of water in rectangular micro-channels.

Chung *et al.* [12] numerically predicted the pressure drop for a single drop passing through a 5:1:5 contraction-straight narrow channel-expansion flow domain, using a Finite Element - Front Tracking Method. They study the effect of drop size, capillary numbers in the range of $0.001 \leq Ca \leq 0.01$ and viscosity ratio's in the range of $0.01 \leq \lambda \leq 100$. They found that the excess pressure drop (ΔP^+), with respect to single phase flow was directly proportional to λ , and inversely proportional to Ca . Shirani and Masoomi [48] perform extensive numerical studies on the motion

on drops on channels, for a Reynolds number Re , ranging from $24 \leq Re \leq 1800$, capillary numbers $0.014 \leq Ca \leq 0.219$. They found that for small Ca , the deformation of the drop does not depend on the capillary numbers, but it is a large function of Ca , when it is large.

1.2.2 Studies on drop dynamics in Microfluidic Junctions

Lehansky and Pismen [34] use a 2D model, and lubrication approximation, in the range of small capillary numbers to propose a mechanism for droplet breakup in a symmetric (daughter channels of equal length) microfluidic T-junction driven by pressure decrement in a narrow gap between the droplet and the channel wall. Their theory, though formally valid for $Ca^{1/5} \ll 1$, approximates very well with numerical results, when extrapolated to moderate values of Ca . Jullien *et al.* [33] have performed experimental studies of droplet breakup in microfluidic T-junctions for capillary numbers in the range $4 \times 10^{-4} \leq Ca \leq 2.5 \times 10^{-1}$, and introduce the concept of critical droplet extension, to describe drop breakup in small and moderately small capillary numbers. Their results were consistent with the 2D-drop breakup theory presented by Lehansky and Pismen [34].

Graaf *et al.* [18], created a model cross-flow membrane emulsification system, to generate monodisperse hexane droplets, using a perpendicular T-shaped microfluidic junctions, with rectangular cross-section. They studied the drop formation, detachment and proposed a simple model to describe the break-up process, incorporating the flow-rates of the external fluids, and various fluid properties. They then

fit the experimental data with the developed model, to predict the necking time. Christopher and Anna [9] characterize, experimentally the breaking-nonbreaking behavior of droplets containing dilute polymer solution, based on their size and speed, as they enter a T-shaped microfluidic junction, and conclude that visco-elastic drops are less stable than Newtonian droplets of comparable shear viscosity. Based on the drop aspect ratio and the capillary number, they show that there is a distinct boundary between drops that break and those that do not break, and the boundaries are different for Newtonian and visco-elastic liquids. They conclude that drops with aspect ratio's > 1 , always break, while smaller droplets require larger capillary numbers to break. Christopher *et al.* [10] systematically examined droplet collisions at a simple microfluidic T-junction, as a function of drop size, speed and characterized the response for a wide range of droplet sizes and speeds. They use $\lambda = 0.01$, and observe four primary responses of a droplet pair approaching the downstream T-junction: (1) no collision, (2) coalescence, (3) slipping, and (4) splitting. Their experiments concluded that low collision speed, not too small droplet sizes, are favorable for coalescence, where local curvature of the colliding droplets at the point of collision, and the viscosity ratios determine the critical capillary numbers for coalescence.

Garstecki *et al.* [30] describe the process of formation of droplets and bubbles in microfluidic T-junction geometries, and provide a scaling relationship to predict the size of the resulting droplets. They conclude that at small capillary numbers, the dynamics of break-up of immiscible threads in T-junctions is dominated by the pressure drop across the droplet or bubble as it forms, and size of the droplets or

bubbles is determined solely by the ratio of the volumetric rates of flow of the two immiscible fluids. They observe a critical value of capillary number ($Ca \sim 10^{-2}$), above which the shear stresses start to play an important role in the process of breakup. De Menech *et al.* [36], in their numerical studies on the dynamics of breakup of streams of immiscible fluids in confined microfluidic T-junction, they identify three distinct regimes of droplet formation: squeezing, dripping, and jetting, which give a deeper understanding of the emulsification process. They identify the squeezing mechanism of breakup as being specific to microfluidic systems, and conclude that breakup in the squeezing regime is driven chiefly by the buildup of pressure upstream of an emerging droplet and that the dynamics of breakup are influenced only very weakly by the value of the capillary number.

Tan, Cristini and Lee [53] designed microfluidic cross-junctions, and used the junction geometries, in addition to the flowrates, to generate controlled droplet sizes. They studied orifices connected to a long straight channel, orifice connected to a short channel, with subsequent rectangular expansion, and an orifice connected to a expansion nozzle. They generate monodispersed primary droplets and monodispersed submicron satellite droplets. Nisisako and Torii [40] used microfluidic large-scale integration on a chip, with 128 cross-junctions, for the mass production of monodisperse emulsion droplets and particles. Luo *et al.* [52] exploited the symmetrical flow route of perpendicular rupturing to generate monodisperse oil in water and water in oil emulsions, using a cross-junction microfluidic device. They studied the formation mechanism of plug flow, the influence of oil/water flow ratio on the shape of the interface, and developed a quantitative equation to predict the plug

length, which is consistent with the experimental results.

Cubaud [14] experimentally studied the dynamic response of a highly viscous droplet to a sharp increase in the surrounding liquid velocity in a square microchannel junction. He created a large velocity contrast between the front and the rear of the droplets by locally injecting a continuous phase from symmetric side channels. Their study shows that microfluidic confinement introduces specific length scales, and, the initial drop shape is shown to play a major role in droplet deformation and breakup. In the asymptotic regime associated with large λ their results suggest that confined relaxation is dominated by the viscosity of the droplet, μ_1 , while confined stretching is relatively independent from μ_1 . Yeh and Lin [66] have used a microfluidic chip containing a cross-junction channel for the manipulation of UV-photopolymerized microparticles. By controlling the relative flow rates in the central and lateral channels, they could control the size of the resulting hydrogel droplets in the range of 75 to 300 μm . They experimentally found that the size of the drops increased with an increase in the average velocity of the dispersed phase flow and decreased with the average velocity increase of the continuous phase flow.

Wu *et al.* [65] applied an improved lattice Boltzmann method to study droplet formation in an immiscible liquid-liquid multiphase flow in a cross-junction microchannel. Their numerical results compared well with experimental results for various inlet velocities. They found capillary number to be an influencing factor in determining the size of the resulting droplet.

1.3 Summary and Layout of Present Thesis

The current thesis considers the dynamics of a droplet moving in confined geometries in Stokes flow. More specifically we study the interfacial dynamics of droplets in (a) a T-Junction and (b) a cross-Junction, using a three-dimensional Spectral Boundary Element algorithm [61] and present our analysis on how the presence of intersecting flows, affects the drop velocities and deformation. We analyze the pressure drop caused by the presence of a single droplet in our geometries, and how the drop length variations affect the pressure gradient. The thesis builds in large part on the studies done by Dimitrakopolous *et al.* [58, 51, 59, 60, 61, 62], and presents the droplet shape fluctuations, the effect of the junctions on the droplet deformation, velocity, pressure-drop and compares the results with the drop motion in a straight square channel, under similar external shear and other physical conditions. These geometries, in modified form are commonly found both in the real-world engineering applications of microfluidics and also in biological fluid/blood pathways like the tortuous networks of blood-vessel in the animal body. Our studies can help partly demystify the significant challenge of understanding the role of shape in various biological, and industrial processes, and help formulate specifications for these systems. By modifying the boundary conditions suitably, these geometries can also be used to study the self-sorting patterns [1]. Though at first glance, T-junctions seem similar to that of cross-junctions, they represent an important difference in lack of symmetry. Inherent symmetry makes it relatively easier to predict the movement of spheres, but non-spherical particles may align or tumble in the presence of

external flow. Non-symmetric conditions are common place in biological systems, for example when particles flow through complex geometries like those in filtering organs, liver, spleen, or when bifurcations in the blood vessels are encountered.

The present thesis is divided into three chapters. After discussing some applications of deformable soft particles and a brief history of the development of the theoretical and computational tools for understanding the droplet dynamics in the introductory chapter, the specific underlying mathematics, including the boundary integral formulation, the spectral methods used, dimensional analysis, and integration methods are discussed in Chapter 2, and finally, we present the current research problem, and discuss our results in Chapter 3.

Chapter 2

Mathematical Formulation

2.1 From Stokes equations to Boundary Integral equations

When the Reynolds number is sufficiently small, the inertial terms in the Navier-Stokes equations are neglected and the flow is governed by Stokes equations

$$\nabla \cdot \boldsymbol{\sigma} \equiv -\nabla p + \mu \nabla^2 \mathbf{u} = 0 \quad (2.1)$$

and the continuity equation

$$\nabla \cdot \mathbf{u} = 0 \quad (2.2)$$

where $\boldsymbol{\sigma}$ represents the stress tensor, p is the dynamic pressure, μ is the viscosity of the fluid and \mathbf{u} is the velocity vector.

By introducing the fundamental solutions S_{ij} and T_{ijk} for the three-dimensional Stokes equation (2.1) and the continuity equation (2.2), and then integrating over a volume of fluid bounded by a surface S_B shown in figure 2.1a, the velocity at a point \mathbf{x}_0 on the surface is expressed as the following Boundary Integral equation (BIE),

$$u_i(\mathbf{x}_0) = -\frac{1}{4\pi\mu} \int_{S_B} (S_{ij}(\hat{\mathbf{x}})f_j(\mathbf{x}) - \mu T_{ijk}(\hat{\mathbf{x}})u_j(\mathbf{x})n_k(\mathbf{x})) dS \quad (2.3)$$

This equation relates the velocity \mathbf{u} at each point \mathbf{x}_0 along the boundary S_B by the surface integral of the stress and velocity over all the points \mathbf{x} on the same boundary.

The normal vector \mathbf{n} points into the domain surrounded by the boundary S_B while

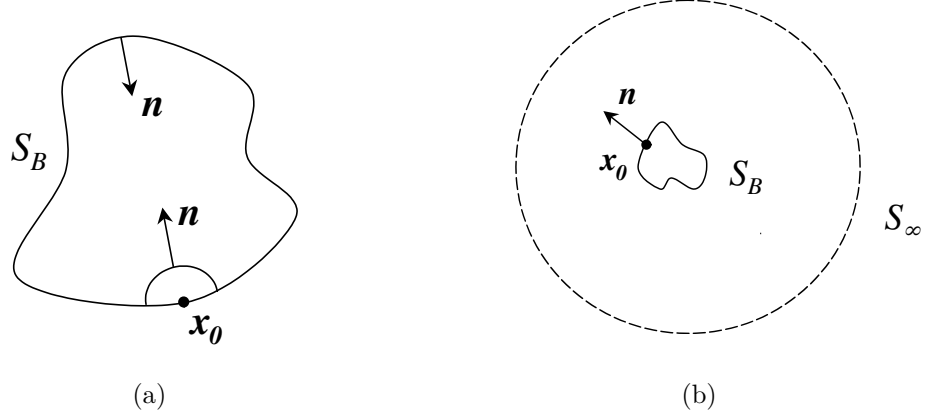


Figure 2.1: Illustrations for the geometry of the BIEs (2.3) and (2.6).

the force vector \mathbf{f} is defined by $f_j(\mathbf{x}) = \sigma_{jk}(\mathbf{x})n_k(\mathbf{x})$. The fundamental solution for the velocity S_{ij} and the corresponding stress T_{ijk} are given by

$$S_{ij} = \frac{\delta_{ij}}{r} + \frac{\hat{x}_i \hat{x}_j}{r^3} \quad (2.4)$$

$$T_{ijk} = -6 \frac{\hat{x}_i \hat{x}_j \hat{x}_k}{r^5} \quad (2.5)$$

A detailed derivation may be found in Pozrikidis [41].

Equation (2.3) can be named as the “inner” equation because it solves for the fluid flow inside a specific boundary S_B shown in figure 2.1a. An “outer” equation can be derived to express the flow field outside a boundary S_B shown in figure 2.1b.

It is given by

$$\mathbf{u}(\mathbf{x}_0) - 2\mathbf{u}^\infty(\mathbf{x}_0) = -\frac{1}{4\pi\mu} \int_{S_B} (\mathbf{S} \cdot \mathbf{f} - \mu \mathbf{T} \cdot \mathbf{u} \cdot \mathbf{n}) dS \quad (2.6)$$

where \mathbf{u}^∞ is the fluid velocity far from the surface boundary S_B and the normal vector \mathbf{n} points into the flow (i.e., out of the boundary S_B).

2.2 BIE for a free suspended drop

Consider the case of a droplet with density ρ_1 and viscosity $\mu_1 = \lambda\mu$ suspended in an infinite fluid with density ρ_2 and viscosity $\mu_2 = \mu$, as illustrated in figure 2.2. The interfacial tension γ is assumed to be constant while \mathbf{u}^∞ is the undisturbed flow velocity. The magnitude of the gravity acceleration is g . The normal vector \mathbf{n} points into the fluid, i.e., outside the interface S_B .

The interior fluid is driven to flow by the exterior flow. The “inner” and “outer” equations (2.3) and (2.6) now apply to the interior and exterior domains, respectively. The “inner” equation has to change sign due to the direction of the normal vector. After subtracting equation (2.3) from equation (2.6), the velocity of the point \mathbf{x}_0 on the interface S_B is expressed as

$$\begin{aligned} & (1 + \lambda)\mathbf{u}(\mathbf{x}_0) - 2\mathbf{u}^\infty(\mathbf{x}_0) \\ &= -\frac{1}{4\pi\mu} \int_{S_B} (\mathbf{S} \cdot \Delta\mathbf{f} - \mu(1 - \lambda)\mathbf{T} \cdot \mathbf{u} \cdot \mathbf{n}) dS \end{aligned} \quad (2.7)$$

where the velocity \mathbf{u} and the jump of the interfacial stress $\Delta\mathbf{f}$ come from the interfacial boundary conditions:

$$\mathbf{u} = \mathbf{u}_1 = \mathbf{u}_2 \quad (2.8)$$

$$\Delta\mathbf{f} \equiv \mathbf{f}_2 - \mathbf{f}_1 = \gamma(\nabla \cdot \mathbf{n})\mathbf{n} + (\rho_2 - \rho_1)(\mathbf{g} \cdot \mathbf{x})\mathbf{n} \quad (2.9)$$

where the subscripts “1” and “2” represent the internal and external flow, respectively. If $\Delta\mathbf{f}$ is known, equation (2.7) becomes a Fredholm integral equation of the second kind in solving for the interfacial velocity \mathbf{u} .

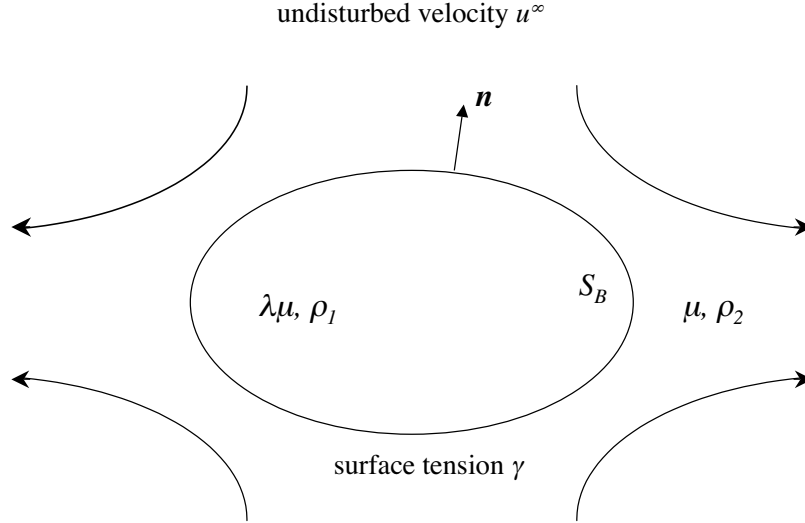


Figure 2.2: Illustration of a droplet freely suspended in an infinite fluid.

2.3 BIE for a drop in a confined domain

Here, we consider the situation where a drop is suspended in an external fluid enclosed by an outer solid boundary (figure 2.3), and discuss the construction of the Boundary Integral Equations for it.

As shown in figure 2.3, a drop with viscosity $\lambda\mu$ and density ρ_1 is suspended in a rectangular channel. The fluid external to the drop has viscosity μ and density ρ_2 while far from the droplet it shows undisturbed velocity \mathbf{u}^∞ and stress \mathbf{f}^∞ . We denote the interface between the drop and the external fluid as Γ , the boundary surface as S_2 , which is composed by S_2^f and S_2^w . S_2^f is a fluid boundary and it is assumed to be far away from the drop. S_2^w refers to the rest solid boundary.

The surface tension on the interface Γ is γ and the magnitude of the gravity acceleration is g . We also denote \mathbf{u}_1 and \mathbf{u}_2 as the flow velocity inside and outside

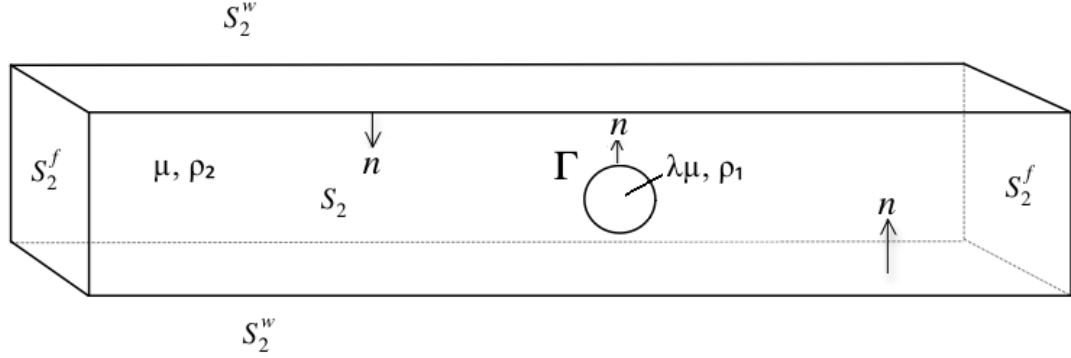


Figure 2.3: Illustration of drop suspended in the fluid inside a rectangular channel.

of the drop, respectively. The boundary conditions on surface S are

$$\mathbf{u}_2 = 0 \quad \text{on boundary } S_2^w \quad (2.10)$$

$$\mathbf{u}_2 = \mathbf{u}^\infty \quad \text{or} \quad \mathbf{f}_2 = \mathbf{f}^\infty \quad \text{on boundary } S_2^f \quad (2.11)$$

The boundary conditions on Γ are given by equations (2.8) and (2.9).

By applying the governing equation (2.3) on the fluid flow both inside and outside the drop, and then performing a subtraction between the two equations, a general Boundary Integral equation for both flow regions can be derived as

$$\begin{aligned} \Omega \mathbf{u}(\mathbf{x}_0) &= - \int_{S_2} [\mathbf{S} \cdot \mathbf{f}_2 - \mu \mathbf{T} \cdot \mathbf{u}_2 \cdot \mathbf{n}] dS \\ &\quad - \int_{\Gamma} [\mathbf{S} \cdot \Delta \mathbf{f} - (1 - \lambda) \mu \mathbf{T} \cdot \mathbf{u} \cdot \mathbf{n}] dS \end{aligned} \quad (2.12)$$

where the subscripts “1” and “2” refer to fluids inside and outside of the drop, respectively. In the second term on the right-hand side, the velocity is $\mathbf{u} = \mathbf{u}_1 = \mathbf{u}_2$. For points on Γ , $\Omega = 4\pi(1 + \lambda)\mu$; for points on S_2 , $\Omega = 4\pi\mu$. A system of Fredholm integral equations of mixed kinds is formed due to the different boundary conditions.

2.4 Spectral element formulation

The Boundary Integral equations are solved using the Spectral Boundary Element method as described in Wang and Dimitrakopoulos [61, 21]. Its accuracy, efficiency and convergence have been demonstrated in applications involving rigid particles, deformable droplets and interacting particles. Dimitrakopoulos and Higdon employed both the 2D [22] and 3D [23, 24, 25, 26, 19] Boundary Element methods in studies on the displacement of droplet from solid surfaces in Stokes flows.

According to this method, the boundary is divided into a moderate number N_E of surface elements, each of which is mapped onto a two-dimensional domain in terms of the parametric variables ξ and η . The variables are zeros of orthogonal polynomials, such as Legendre, Chebyshev or Jacobi polynomials, on $[-1, 1]$. If N_B basis points are used, then the geometry \mathbf{x} can be represented by

$$\mathbf{x}(\xi, \eta) = \sum_{i=1}^{N_B} \sum_{j=1}^{N_B} \mathbf{x}(\xi_i, \eta_j) h_j(\eta) h_i(\xi) \quad (2.13)$$

where $h_i(\xi)$ and $h_j(\eta)$ are the $(N_B - 1)$ -order Lagrangian interpolant polynomial. The physical variables \mathbf{u} and \mathbf{f} are represented similarly.

The discretized expressions for the geometry and the physical variables are substituted into the Boundary Integral equations, and it is required that the integral equations be satisfied at the discrete set of basis points $\mathbf{x}_0(\xi_i, \eta_j)$ (where $i, j = 1, \dots, N_B$) on each spectral element. This yields a linear system of $3N_E N_B^2$ algebraic equations

$$\mathbf{u} = \mathbf{A}\mathbf{f} + \mathbf{B}\mathbf{u} \quad (2.14)$$

The system matrices \mathbf{A} and \mathbf{B} are defined as integrals of the kernels \mathbf{S} and \mathbf{T} (see equations (2.4) and (2.5)) and the basis functions over the set of the surface elements. The numerical integration is performed by Gauss-Legendre quadrature with the aid of variable transformations.

The BIEs, combined with the boundary data at the $N_E N_B^2$ basis points, yield, for a known interface, a consistent set of $3N_E N_B^2$ equations in $3N_E N_B^2$ unknowns which is solved using Gaussian elimination.

2.5 Problem parameters and dimensionless analysis

The problem of interfacial dynamics in Stokes flow is mainly governed by two dimensionless numbers: the viscosity ratio λ and the capillary number Ca given by

$$\lambda = \frac{\mu_1}{\mu} \tag{2.15}$$

$$Ca = \frac{\mu U}{\gamma} \tag{2.16}$$

where μ_1 is the viscosity of the fluid inside the drop, μ is the viscosity of the imposed flow, and γ is the surface tension on the interface, and U is the average fluid channel velocity in a straight channel, in the absence of drop.

The capillary number Ca measures two competing forces: the viscous force and the surface tension force. The viscous stress imposed on the interface by the exterior flow induces the flow inside the drop and causes the interfacial deformation, while the surface tension force resists the deformation. Steady state is reached when the surface tension forces balances the viscous forces so that the droplet deformation ceases. The flow velocities, are given in terms of shear rate, and are depicted by

X_{sh} in the channel along x -axis, and by Y_{sh} in the channel along the y -axis.

Figure 2.4 illustrates a geometry used for a cross-junction with non-zero bend radius ($r_b > 0$), where, the bends can be visualized as the quarter cylinders, placed appropriately. Figure 2.4 becomes a right angled cross-junction when, the bend radius, $r_b = 0$, and can be visualized as a T-junction, when the upper channel is cut, and the left and right channels are joined by a straight top-plate. When we have a cross-junction, the channels along the x -axis are the primary channels (drop moves from left channel to the right channel), and those along y -axis are the lateral channels (no drop in the lateral channels).

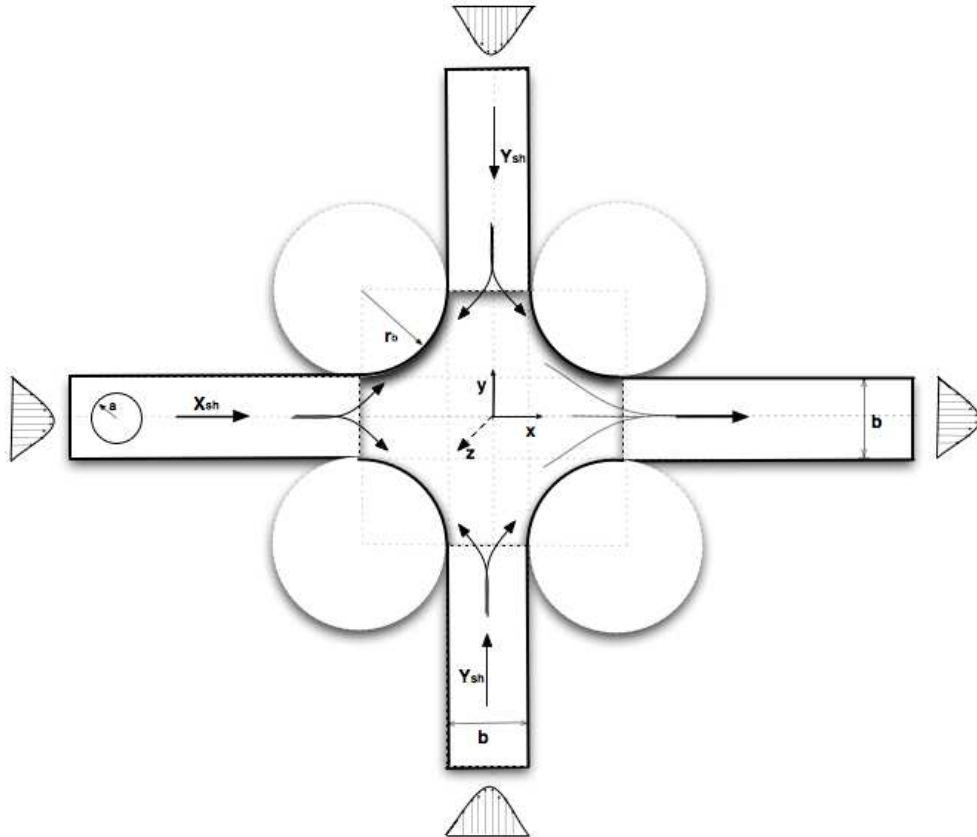


Figure 2.4: 2D illustration for the cross-junction geometry.

In our study, we start with a spherical droplet at time $t = 0$, and fix its radius as $a = 0.7$. As seen in figure 2.4, the flow velocities are given in terms of shear rate, and are depicted by X_{sh} for the channel along x -axis, and by Y_{sh} in the channel along the y -axis. We control the smoothness of the junction by defining bend radius r_b , a right-angled junction corresponds to the case $r_b = 0$. All smooth intersections in this study use $r_b = 2$. For all the geometries in this thesis, we use a square cross-section with half-length $b/2 = 1$.

2.6 Boundary Conditions

We use velocity boundary conditions in the problems discussed in this thesis. The steady flow profiles for straight rectangular channels are found by the method of separation of variables, and are applied as the initial velocity conditions at all the fluid boundaries.

$$\mu \left(\frac{\partial^2}{\partial y^2} + \frac{\partial^2}{\partial x^2} \right) \mathbf{u} = -K - \rho g \sin(\beta) \quad (2.17)$$

Yih [67] derives the boundary conditions for the case of flow along increasing x . Figure 2.5 shows the cross section of a typical rectangular channel. The governing equations for flow along increasing x can be represented by equation 2.17 where, β represents the angle of inclination between the x -axis and the horizontal plate, K is $-\partial p/\partial x$, a constant but ρ may be a function of z . The solution of equation 2.17 can be written as

$$u = u_c + u_p \quad (2.18)$$

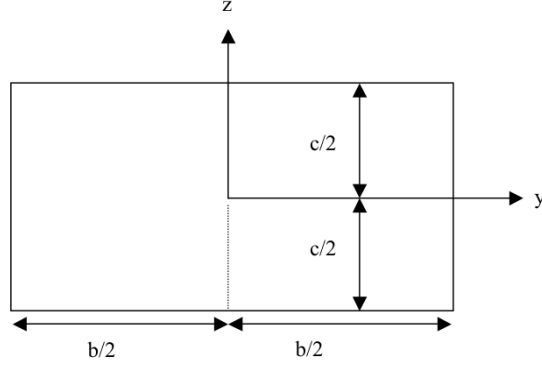


Figure 2.5: Coordinates for a rectangular cross-section, flow symmetric with respect to both y and z axis

When the flow is symmetric with respect to both y and z axis, the particular solution u_p can be expressed by equation 2.19, and the complementary solution u_c by equation 2.19

$$u_p(z) = \frac{1}{2\mu}(K + \rho g \sin(\beta)) \left(\frac{c^2}{4} - z^2 \right), \quad (2.19)$$

$$u_c(z) = \sum_{n=1}^{\infty} A_n \cosh \frac{(2n-1)\pi y}{c} \cos \frac{(2n-1)\pi z}{c}, \quad (2.20)$$

The A 's in equation 2.20 can be determined by equation 2.21 The velocity profile for the case in this thesis, with $b=c=2$ is shown in figure 2.6

$$A_n \cosh \frac{(2n-1)\pi b}{2c} = (-1)^n \frac{c^2}{2\mu\alpha_n^3} (K + \rho g \sin \beta), \quad (2.21)$$

$$\alpha_n = \frac{(2n-1)}{\pi}.$$

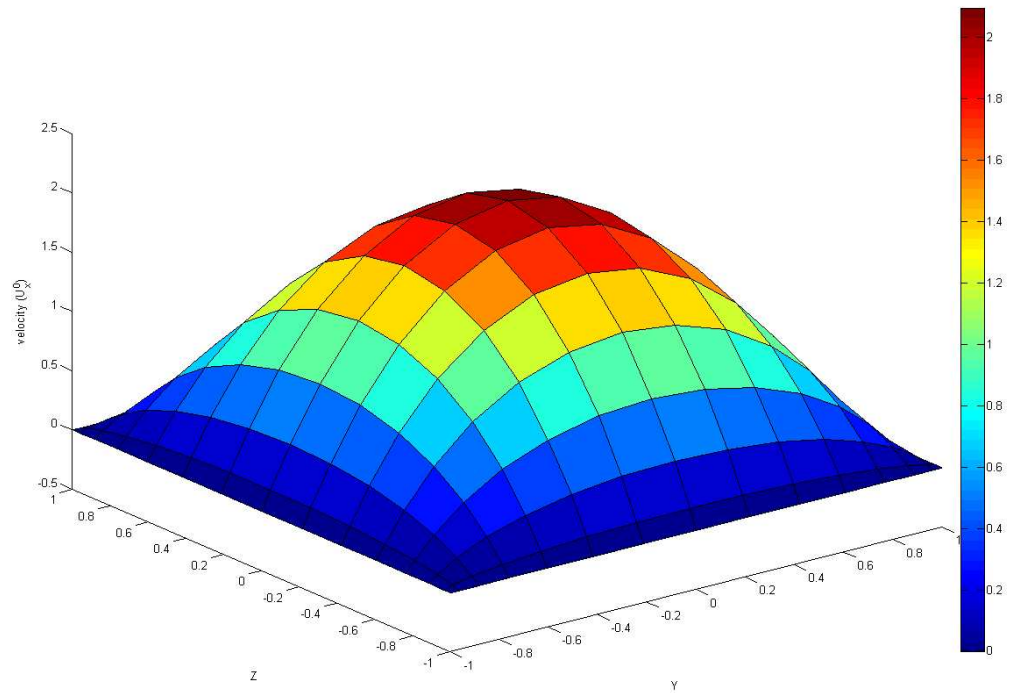


Figure 2.6: Velocity boundary conditions for square cross-sections of length 2, as applied at the fluid boundaries, for flow along increasing- x direction.

Chapter 3

Results and Discussion

As discussed in Chapter 1, the study of drop dynamics in T-junctions and cross-junctions, among other things can differ in the presence (or absence) of symmetry. We say can ‘differ’, because the symmetry in the cross-junctions too, depends on the relative direction of flows and the position of the droplet. In our study, we consider, microfluidic junctions with intersecting flows along x and y axis. It is important to note that, we ignore gravity in our simulations. We determine drop motion for the cases of varying shear rates in the channels along x and y -axis, that lead to the cross-junction. For all the computations in this thesis, we fix the capillary number to be $Ca = 0.1$. We initiate the computations with a spherical droplet of radius $a=0.70$, total length of the geometry along x -axis is 18 units, and total length of the geometry along y -axis is 10 units. We use square cross-sections of side $b = 2$ units, for channels along both the x and y directions. All intersecting geometries in this thesis, when smooth have a bend radius r_b of 2 units. We note that the channel half cross-sectional length $b/2$ is the length scale used throughout our study.

We will divide the current chapter into two sections, based on the junction geometry, one refers to the study of flow in T-junctions and the other towards the study of drop dynamics in cross-junctions.

3.1 Microfluidic Cross-Junctions

All the cross-junctions in this study have three incoming flows, one each along the channels placed at increasing- x , decreasing- y and increasing- y directions. All the three incoming lateral flows then merge into the channel placed along positive, increasing x direction. The drop is always started from an inlet channel placed along the $-x$ direction.

3.1.1 Cross-Junctions with 90° bends (bend radius $r_b = 0$)

In this section we discuss the case of a cross-junction with right-angled bends. Figures 3.1 illustrates the actual geometry used along with the meshing and initial position of the droplet. This geometry can be thought of as four straight, square channels, placed along the x -axis and y -axis, and joined together. The actual junction length ranges from $x = [-9, 9]$, $y = [-5, 5]$, and the cross-section of the channels along x -axis ranges from $y = [-1, 1]$ and $z = [-1, 1]$, and the cross-section of the channels oriented along the y -axis ranges from $y = [-1, 1]$ and $z = [-1, 1]$.

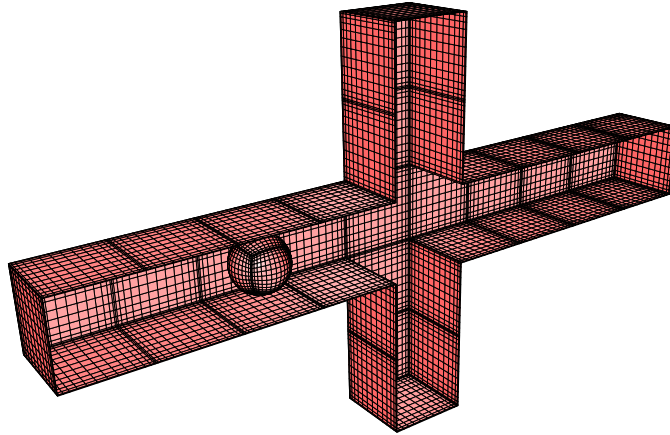
Figure 3.2 gives the drop displacement along the x -axis as a function of time for the case of a cross-junction with bend radius $r_b = 0$, and $r_b = 2$. Figure 3.3 gives the drop velocities for the cases of varying shear in channels along y -axis, and a fixed shear $X_{sh} = 1$ in the x -channel.

Figures 3.3, 3.4 elicit the effect of varying lateral shear rates on the drop velocities, drop length and surface area. We analyze the cases where the lateral shear rate is $Y_{sh} = 0, 0.1, \text{ and } 0.5$. Figures 3.5, 3.6, 3.7 show the effect of varying

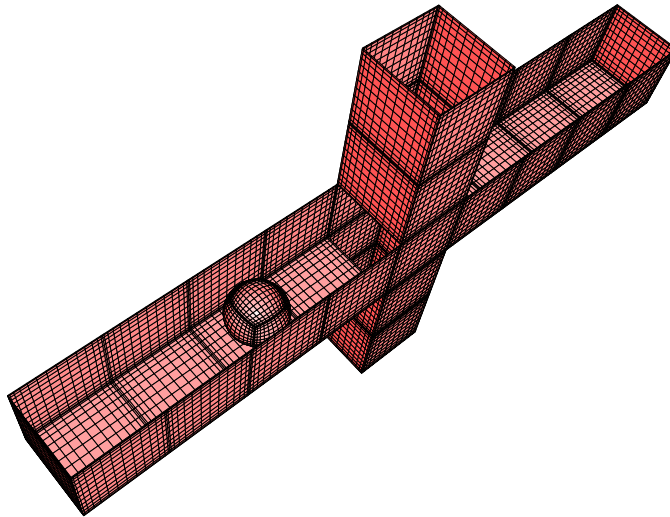
viscosity ratio's, λ , between the drop and the surrounding liquid. We analyze two cases, where $\lambda = 0.2$ and $\lambda = 20.0$.

Figure 3.2 shows that at given time, the drop in the cross-junction with bend radius $r_b = 0$ is ahead of the drop in the bend radius with $r_b = 2$. This can be attributed to the greater junction region in the latter junction. Also to be noted from figure 3.2 is the change in the slopes of the curves, which corresponds to the droplet crossing the junction region and entering the receiver channel, which has a higher bulk velocity. In figure 3.3, the graphs with $Y_{sh} = 0$ represents the case, without any incoming flows in the y -channels. This reduces the problem to the case of an extended external bump, but serves as an important reference to compare our results. As we can see in this case, the drop velocity immediately reaches steady state, and starts to drop as it approaches the junction, starting at $x = -1$, reaches a minima at $x = 0$, starts increasing, and then quickly gains steady state velocity beyond by the time it reaches $x = +1.5$. Points to note in this case is the plot is perfectly symmetrical about the point $x = 0$, i.e., the steady state velocities are the same in both the incoming and outgoing x -channels.

It is also important to note that the steady state velocity for the case of $Y_{sh} = 0$ in figure 3.3, matches exactly with the steady state velocity for drop deformation in a straight channel, under similar conditions. This validates the implementation of boundary conditions in our study. Figure 3.3 says that the greater the lateral shear rates, the greater is the localized velocity gradient in the junction (in this case from $x = -1$ to $x = +1$). This gradient is an important factor as it induces high,



(a) XY view (with front elements removed)



(b) XZ view (with top elements removed)

Figure 3.1: Representative geometry for a cross-junction with bend radius $r_b = 0$.

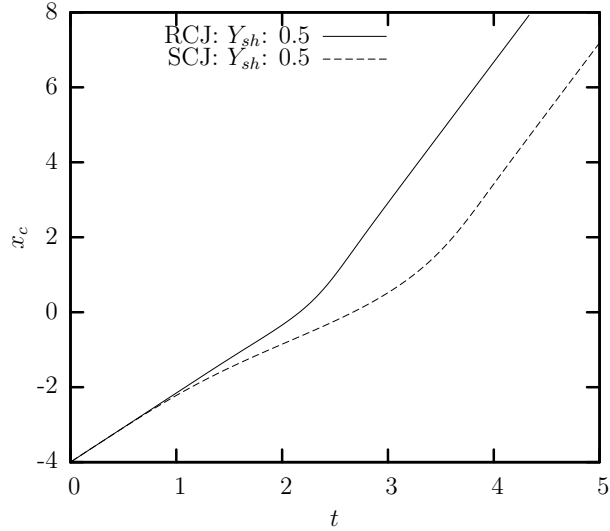


Figure 3.2: Drop displacement along x -axis as a function of time t , in a microfluidic cross-junction, with bend radius $r_b = 0$ and $r_b = 2$, square cross-sectional length $b = 2$, shear rate along x -axis $X_{sh} = 1.0$, shear rate $Y_{sh} = 0.5$ along y -axis, capillary number $Ca = 0.1$ and viscosity ratio $\lambda = 0.2$.

momentary forces on the droplet, which can cause the drop to break, or tumble, or make elongated threads, depending on the capillary number Ca , viscosity ratio, λ and relative shear rates. Also the time required to attain back the steady state seems to be a weak function of the lateral shear rates for the test case of medium capillary number, $Ca = 0.1$ used in the present thesis.

If we compare the x , y , z length of the droplet for a single case, shown in figures 3.4(a-c), we find that the drop maintains YZ -symmetry until it approaches, the junction, at $x = -2$, after which the incoming lateral flows, induce forces in the y -direction, thereby voiding the YZ -symmetry throughout the junction. Interestingly,

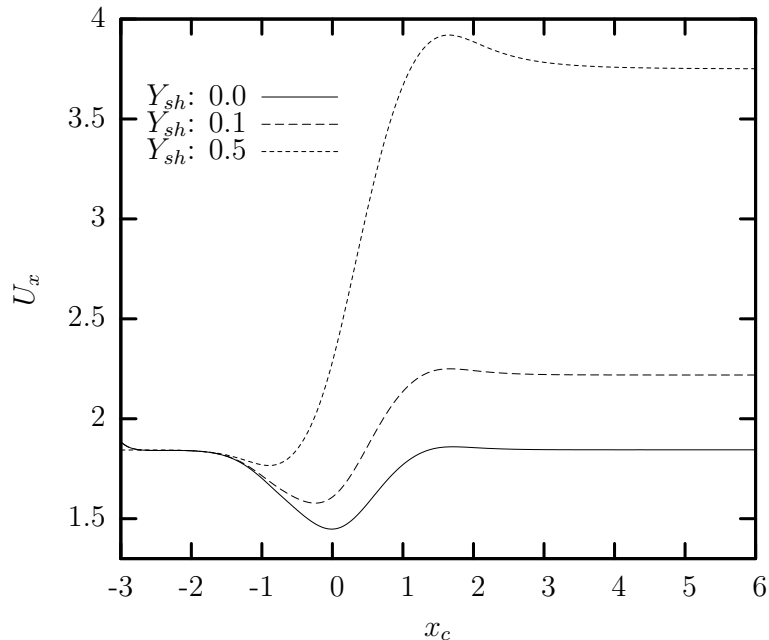


Figure 3.3: Drop velocity along x -axis U_x as a function of drop centroid x_c , in microfluidic cross-junctions with bend radius $r_b = 0$, square cross-sectional length $b = 2$, shear rate along x -axis $X_{sh} = 1.0$, varying shear rate Y_{sh} along y -axis, capillary number $Ca = 0.1$ and viscosity ratio $\lambda = 0.2$.

once the drop passes the junction, it strives to regain the lost symmetry. We observe from figure 3.4(d), that for the test conditions, though the length of the droplet changes considerably along the x , y or z -axes, the total surface area of the drop changes by a maximum of 1% for the case of $Y_{sh} = 0.5$.

Figure 3.5 gives the effects of viscosity on the drop velocities, and as we can see here, at any given position, the drop with the lower viscosity maintains a relatively higher velocity. It must be pointed out though that viscosity seems to affect the velocities very weakly. Figure 3.6 shows the effect of viscosity on the drop length. We

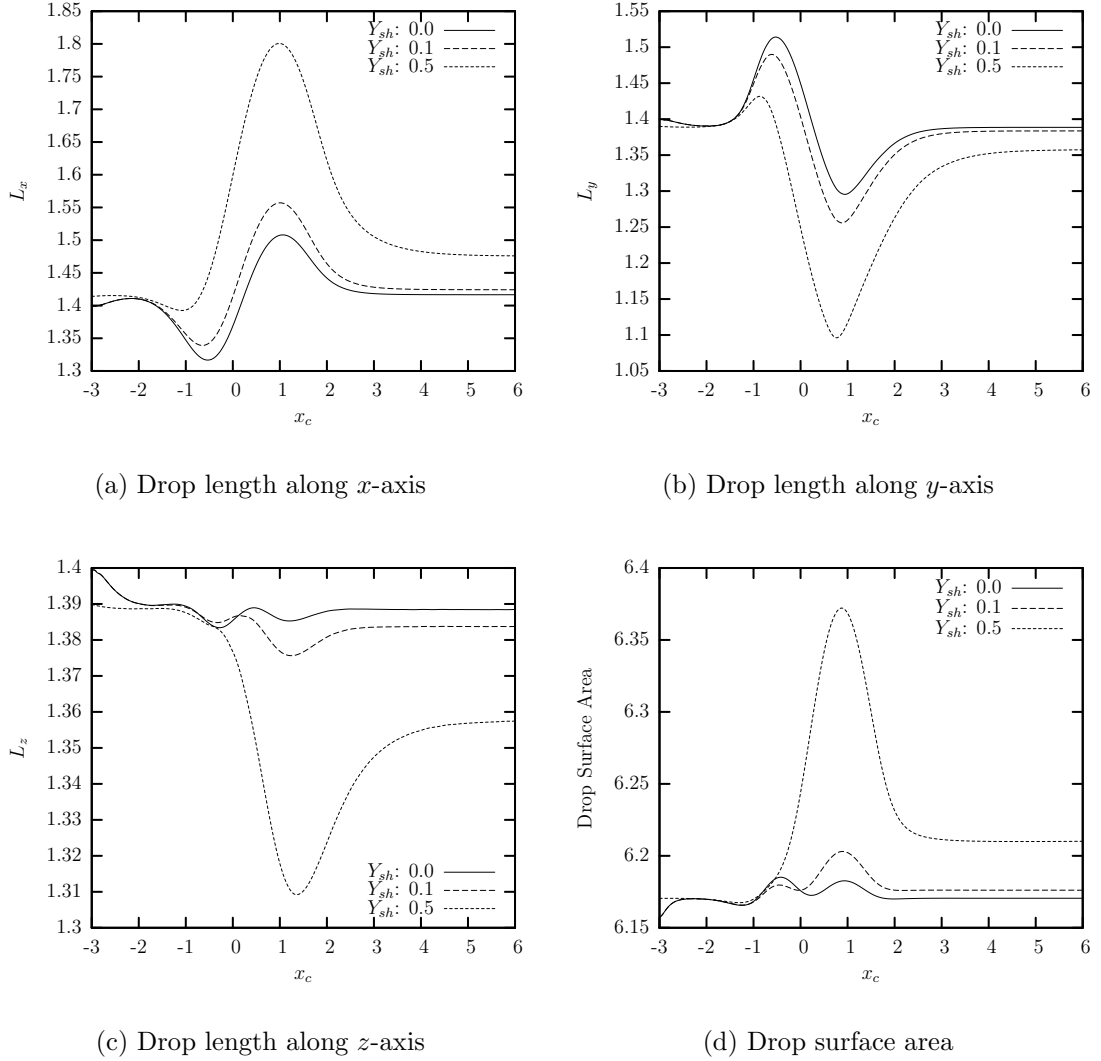


Figure 3.4: Maximum droplet length (L_x , L_y , L_z), along x , y , z -axes respectively, and surface area as a function of drop centroid x_c , in a microfluidic cross-junction, with bend radius $r_b = 0$, square cross-sectional length $b = 2$, shear rate along x -axis $X_{sh} = 1.0$, varying shear rate Y_{sh} along y -axis, capillary number $Ca = 0.1$ and viscosity ratio $\lambda = 0.2$.

observe that viscosity is an important factor in determining the drop deformations, an observation also confirmed by figure 3.7(a), where the peak surface area seems to be about 2% higher for the case with $\lambda = 0.2$, compared with the case $\lambda = 20.0$. Comparing figure 3.7(b), and figure 3.6(a), we find that there seems to be a strong correlation between excess pressure drop at a given spatial coordinate and the drop length at the corresponding position. As we can see from figure 3.7(b), the excess pressure drop increases with the increase in length of the droplet along x -axis, L_x , peaks where the L_x peaks, in the junction, and reaches a steady state when L_x reaches a steady state.

Figure 3.11(c), is a plot of the head and tail length of the droplet along the x -axis. The head length is defined as the maximum of the distance between the centroid of the droplet and the drop interface along the direction of the flow, and similarly tail length is the maximum of the distance between the drop centroid and drop interface against the direction of flow. An interesting fact appears from figure 3.11(c), that the head is always longer than the tail, telling us that the droplet is in the form of a bullet. Also, interesting to note is the observation that the difference in the length of the head and tail is multiplied by a factor, proportional to the increase in the flow-rates in the receiver channel, compared to the feeding channel. This means that almost all the surface area increase in the drop that occurs due to the junction is at its front tip. This could be an important repercussion in areas where mass transport to/from the drop is an important design parameter.

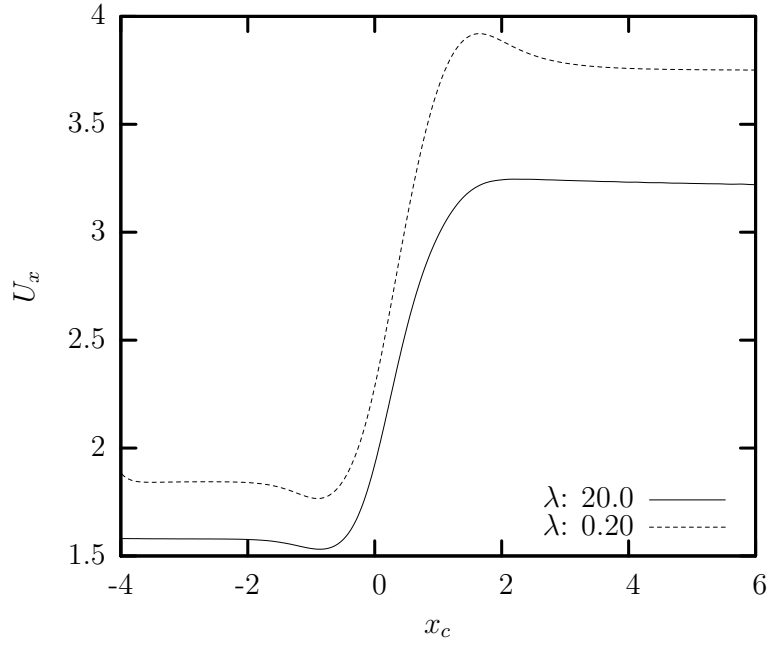
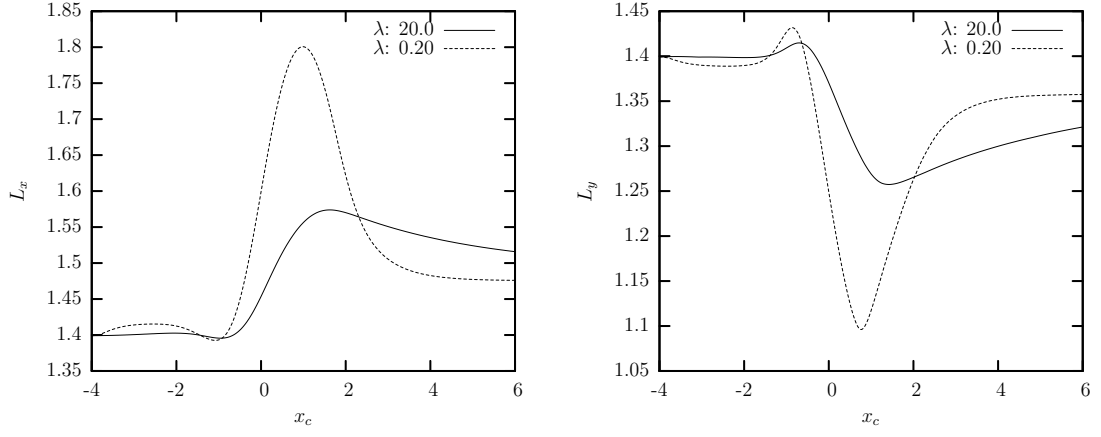
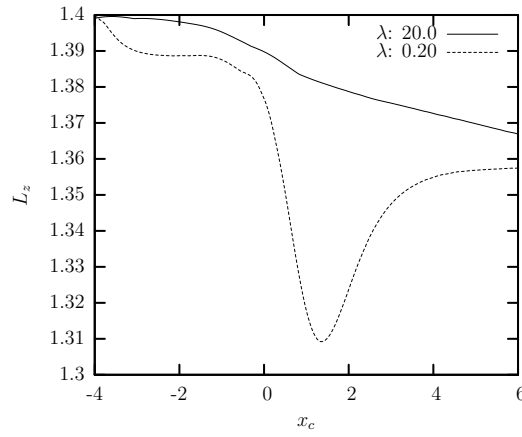


Figure 3.5: Drop velocity along x -axis U_x as a function of drop centroid x_c , for viscosity ratio's $\lambda = 0.2, 20.0$, in a microfluidic cross-junction, with bend radius $r_b = 0$, square cross-sectional length $b = 2$, shear rate along x -axis $X_{sh} = 1.0$, shear rate along y -axis $Y_{sh} = 0.5$, capillary number $Ca = 0.1$.



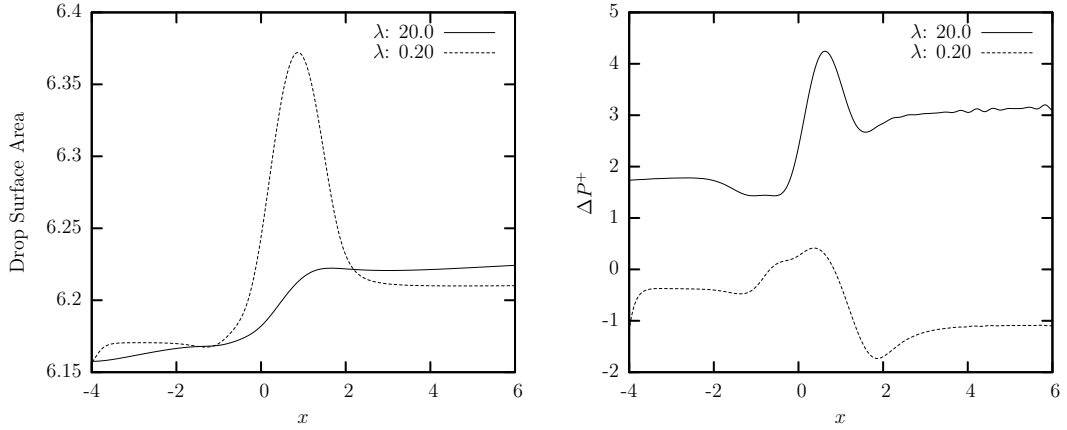
(a) Drop length along x -axis

(b) Drop length along y -axis



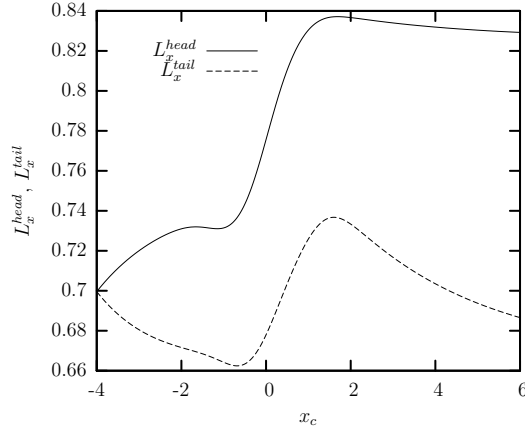
(c) Drop length along z -axis

Figure 3.6: Maximum droplet length (L_x , L_y , L_z), along x , y , z -axes respectively, as a function of drop centroid x_c , for viscosity ratio $\lambda = 0.2$ and $\lambda = 20.0$, in a microfluidic cross-junction, with bend radius $r_b = 0$, square cross-sectional length $b = 2$, shear rate along x -axis $X_{sh} = 1.0$, shear rate along y -axis $Y_{sh} = 0.5$, capillary number $Ca = 0.1$.



(a) Drop surface area

(b) Excess pressure drop along x -axis



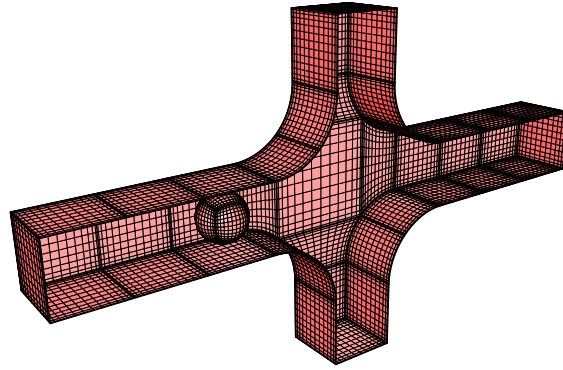
(c) Head and tail length along x -axis

Figure 3.7: (a) Drop surface area as a function of drop centroid x_c , for viscosity ratio $\lambda = 0.2$ and $\lambda = 20.0$ (b) Excess pressure drop as a function of drop centroid x_c , for viscosity ratios $\lambda = 0.2$ and $\lambda = 20.0$ and (c) Droplet head and tail length along x -axis as a function of drop centroid x_c for viscosity ratio $\lambda = 20.0$, in a microfluidic cross-junction, with bend radius $r_b = 0$, square cross-sectional length $b = 2$, shear rate along x -axis $X_{sh} = 1.0$, shear rate along y -axis $Y_{sh} = 0.5$, capillary number $Ca = 0.1$.

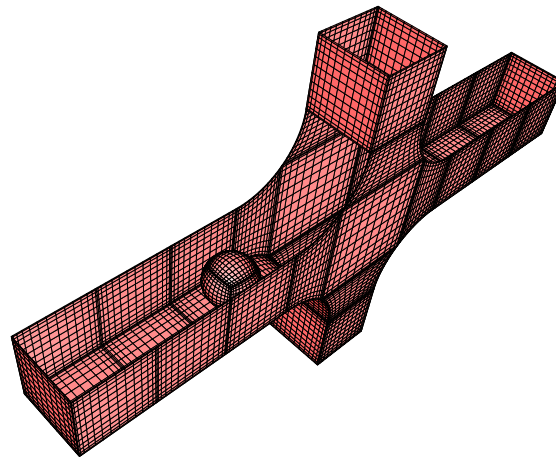
3.1.2 Cross-Junctions with non-zero bend radius ($r_b > 0$)

The smooth bends in the geometry are implemented as quarter cylinders, and we refer the radius of this imaginary cylinder as the bend radius r_b . To maintain the symmetry in the problem, we use the same $r_b = 2$ over all the bends in the geometry. The geometry of the smooth cross-junction used, along with the representative meshing and the initial drop position is shown in figure 3.8. Figures 3.9, 3.10, 3.11 give the different measured properties like the drop velocity, drop length along individual axis, surface area, pressure drop, head and tail length for two different shear rates in the y -direction. Note that because of a non-zero bend radius in this geometry, the junction (region where the drop is directly exposed to the lateral flows) now extends from $x = -3$ to $x = +3$.

Figure 3.9, presents the velocity profile for an initially spherical drop, starting from $x = -4.0$. The graphs seem as expected, with an extended junction area resulting in a more dramatic initial reduction of drop velocities as compared to the right-angled cross-junction. Figure 3.10 shows the length of the maximum droplets along x , y , and z -axis respectively, again for the case of two lateral shear rates of $Y_{sh} = 0$, and $Y_{sh} = 0.5$. Figure 3.11(a) presents the drop surface area with drop position x_c , while figure 3.11(b-c) shows the droplet head and tail length for cases $Y_{sh} = 0.5$ and $Y_{sh} = 0$ respectively. Our previous observation that the difference in the length of the head and the tail are related to the lateral flow rates is corroborated by observing figure 3.11(b-c) where the difference in the length remains the same for the case of $Y_{sh} = 0$.



(a) XY-view (with front elements removed)



(b) XZ-view (with top elements removed)

Figure 3.8: Illustration of geometry for a cross-junction with bend radius $r_b = 2$.

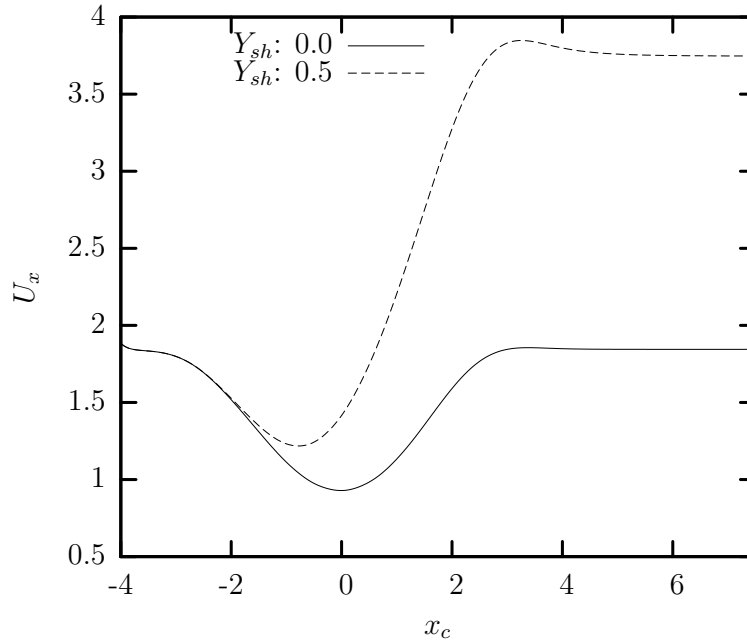
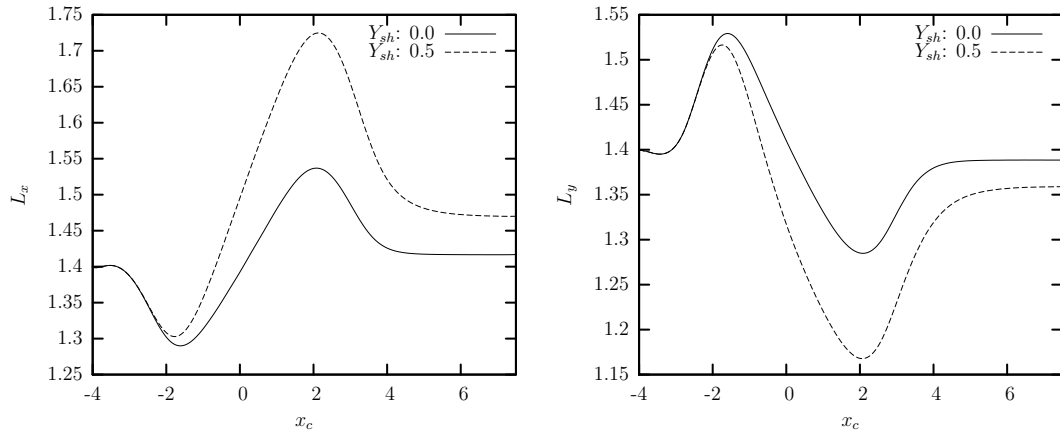


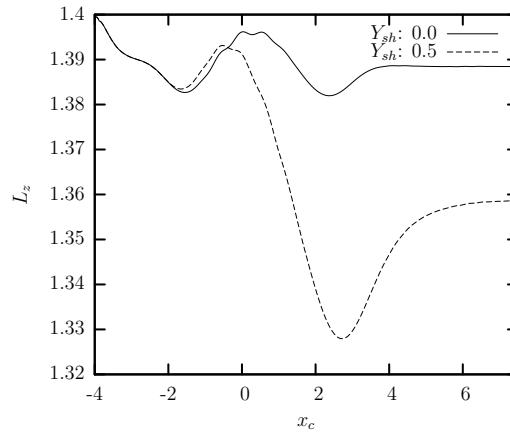
Figure 3.9: Drop velocity, U_x along x -axis, as a function of position x_c , in a microfluidic cross-junction, with bend radius $r_b = 2$, square cross-sectional length $b = 2$, shear rate along x -axis $X_{sh} = 1.0$, varying shear rate Y_{sh} along y -axis, capillary number $Ca = 0.1$ and viscosity ratio $\lambda = 0.2$.

Figures 3.12 and 3.13, compare the measured properties for the two kinds of cross-junctions in this study ($r_b = 0$, $r_b = 2$). As seen from these figures, we note that almost all the measured properties seem to be comparable in both the geometries in the junction region and exactly same both far ahead and far beyond the junction region. We observe that the drop velocities in the junction region for the cross-junction with $r_b = 2$ are always lower than the right-angled cross junction under similar conditions. We can conclude that the junction geometry affects the drop dynamics only in the junction region, albeit weakly.



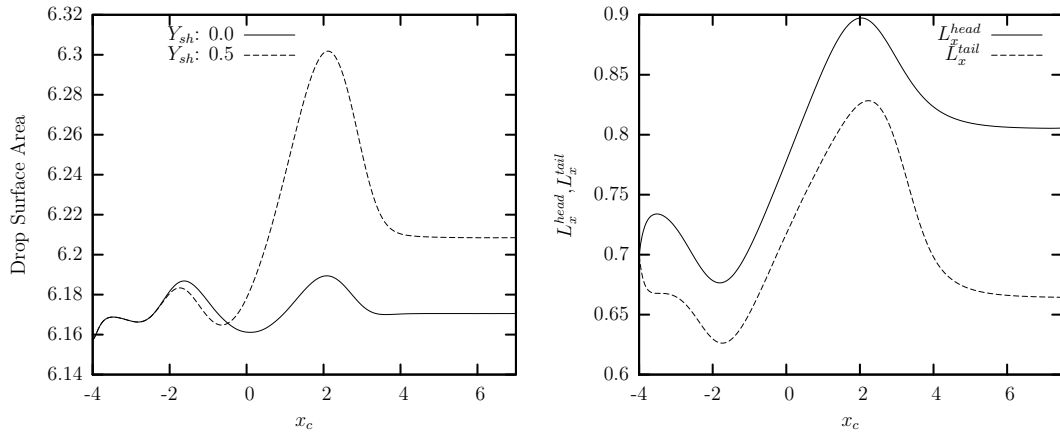
(a) Drop length along x -axis

(b) Drop length along y -axis



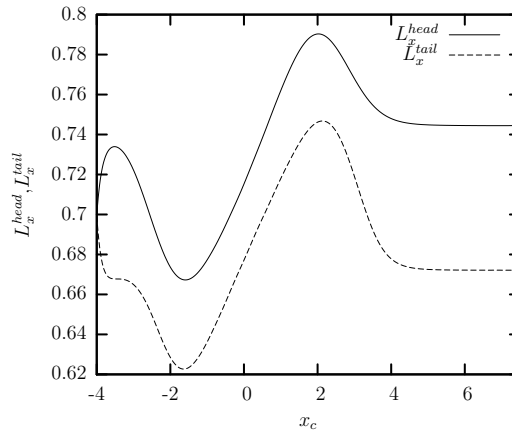
(c) Drop length along z -axis

Figure 3.10: Maximum droplet length (L_x , L_y , L_z), along x , y , z -axes respectively, as a function of drop centroid x_c , in a microfluidic cross-junction, with bend radius $r_b = 2$, square cross-sectional length $b = 2$, shear rate along x -axis $X_{sh} = 1.0$, varying shear rate Y_{sh} along y -axis, capillary number $Ca = 0.1$ and viscosity ratio $\lambda = 0.2$.



(a) Drop surface area

(b) Head and tail length: $Y_{sh} = 0.5$



(c) Head and tail length: $Y_{sh} = 0$

Figure 3.11: (a) Drop surface area (b) Droplet head and tail length along x -axis (c) Droplet head and tail length along x -axis as a function of drop centroid x_c , for shear rate along y , $Y_{sh} = 0$, in a microfluidic cross-junction, with bend radius $r_b = 2$, square cross-sectional length $b = 2$, shear rate along x -axis $X_{sh} = 1.0$, capillary number $Ca = 0.1$ and viscosity ratio $\lambda = 0.2$.

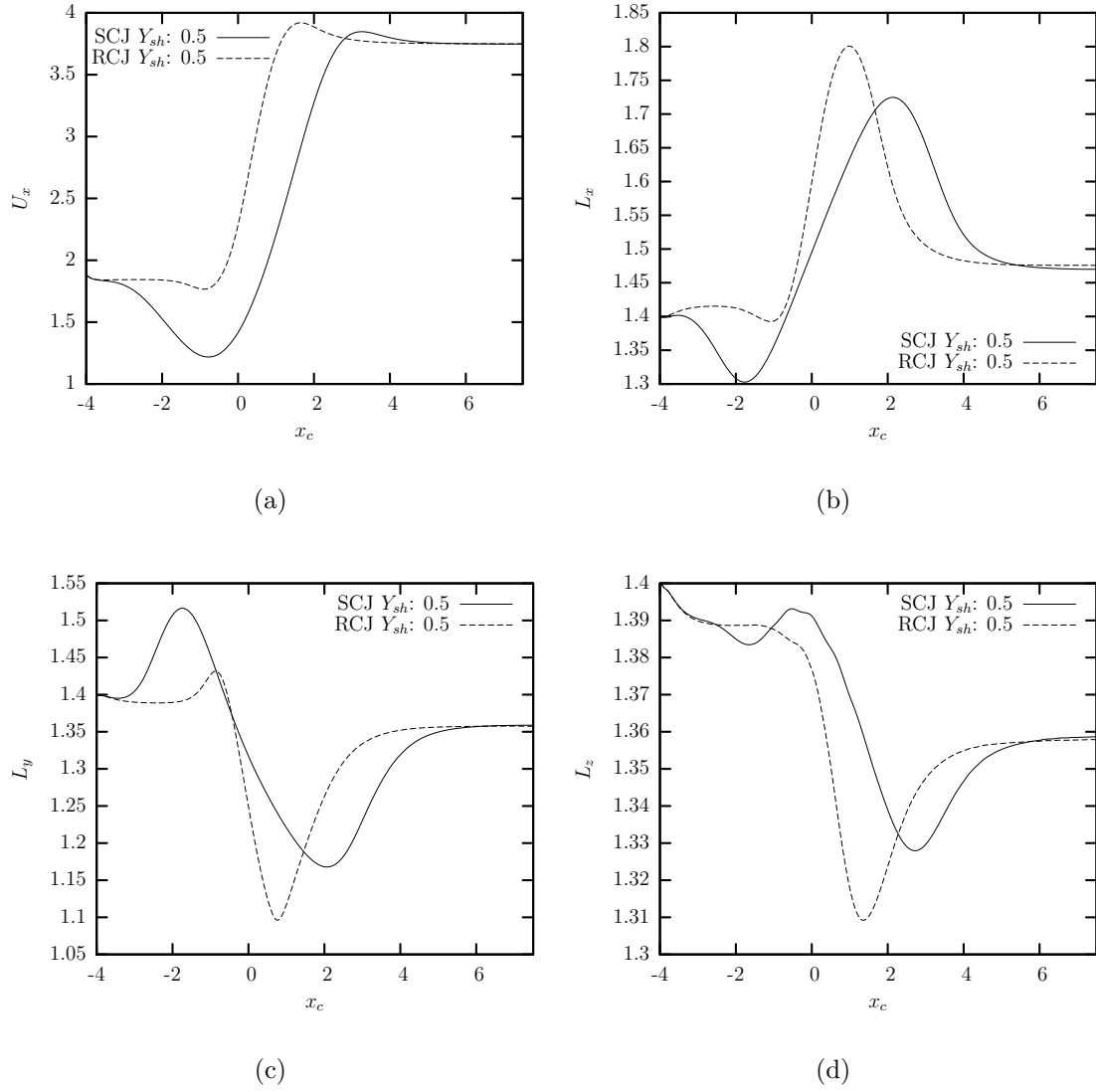


Figure 3.12: Drop velocity U_x along x -axis, maximum drop length (L_x , L_y , L_z) as a function of drop centroid x_c , in microfluidic cross-junctions, with bend radius $r_b = 0$, and $r_b = 2$, square cross-sectional length $b = 2$, shear rate along x -axis $X_{sh} = 1.0$, shear rate along y -axis $Y_{sh} = 0.5$, capillary number $Ca = 0.1$ and viscosity ratio $\lambda = 0.2$.

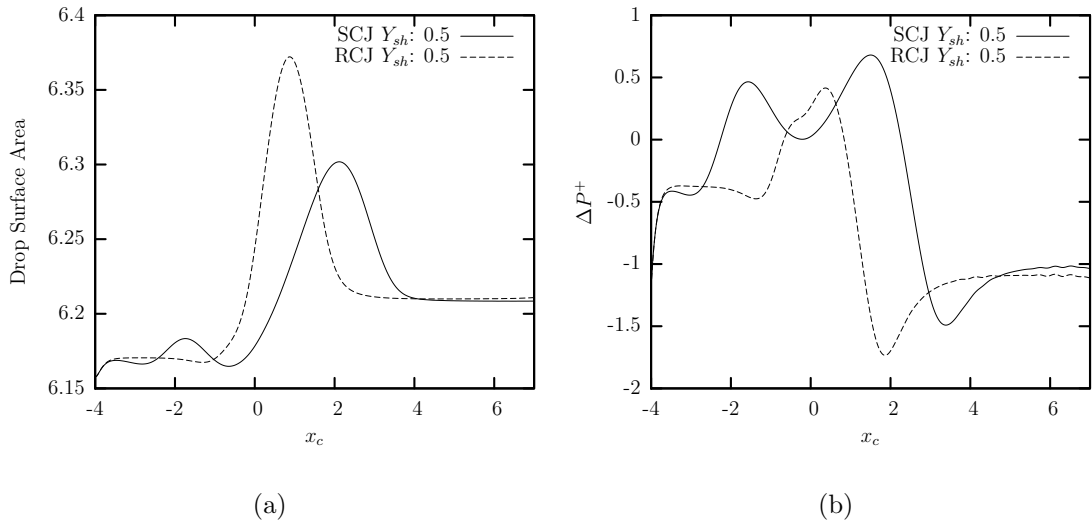
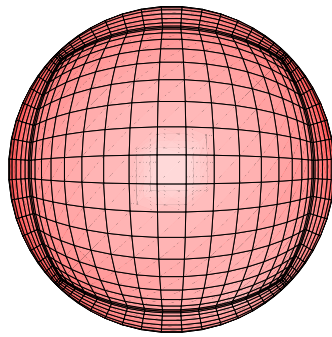


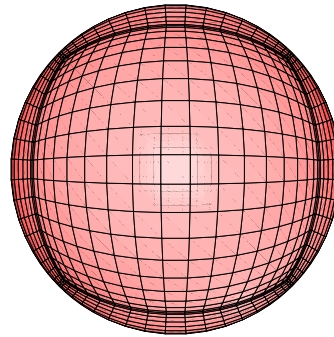
Figure 3.13: (a) Drop surface area as a function of drop centroid x_c , and (b) Excess pressure drop in microfluidic cross-junction, with bend radius $r_b = 0$, and $r_b = 2$, square cross-sectional length $b = 2$, shear rate along x -axis $X_{sh} = 1.0$, shear rate along y -axis $Y_{sh} = 0.5$, capillary number $Ca = 0.1$ and viscosity ratio $\lambda = 0.2$.

Based on the observation from figures 3.12, 3.13, that the measured properties in both the cross-junction geometries used in this thesis are comparable, we plot the droplet snapshots at different spatial positions in the figure 3.14. These figures are plotted for the case of a cross-junction with a bend radius $r_b = 0$, $\lambda = 20.0$ but the trend observed with respect to the shape evolution is applicable to both the geometry configurations.

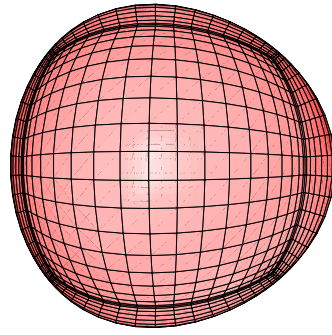
Figure 3.14(c), 3.14(d) is snapshot of the drop configuration at $x_c = -1.073$ (drop has just entered the junction), which shows that the drop deformation along the XZ and XY planes remains almost the same, i.e., we have the YZ symmetry in the system. But as the drop proceeds further into the junction, the lateral flows hit the drop directly, and the symmetry along YZ symmetry is compromised. Finally once the drop crosses the junction, it once again tries to regain the lost YZ symmetry as can be seen from figures 3.14(i) and 3.14(j).



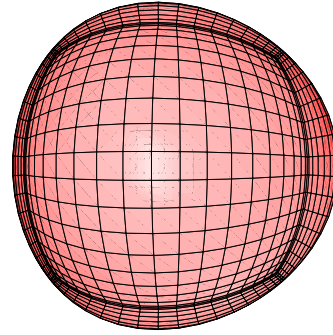
(a) XZ-view: $x_c = -3$ sec



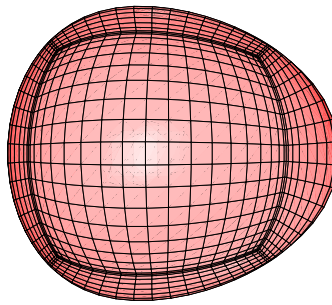
(b) XY-view: $x_c = -3$ sec



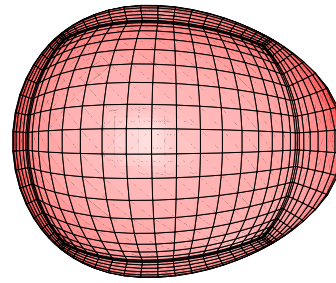
(c) XZ-view: $x_c = -1.073$



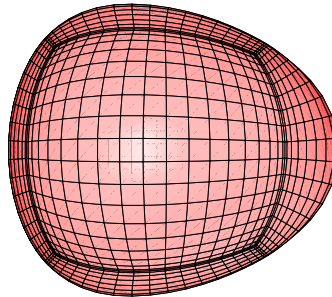
(d) XY-view: $x_c = -1.073$



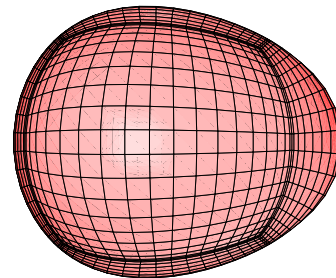
(e) XZ-view: $x_c = 0.855$



(f) XY-view: $x_c = 0.855$



(g) XZ-view: $x_c = 3.538$



(h) XY-view: $x_c = 3.538$

Figure 3.14: Shape evolution of droplet in a microfluidic cross-junction, with bend radius $r_b = 2$, square cross-sectional length $b = 2$, shear rate along x -axis $X_{sh} = 1.0$, shear rate along y -axis $Y_{sh} = 0.5$, capillary number $Ca = 0.1$ and viscosity ratio $\lambda = 20.0$.

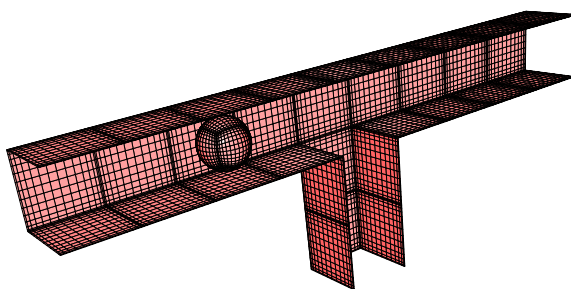
3.2 Microfluidic T-junctions

The T-junction geometries can be viewed as a simplification of the cross-junction, with one less intersecting, lateral channel. All the T-junction geometries in this study have two intersecting flows, one each along increasing- x and increasing- y -axis, both of which merge into a third channel, along increasing- x . As in the case of the cross-junctions, we start our computations, with an initially spherical droplet, of radius $a = 0.7$, and apply the velocity boundary conditions as discussed in section 2.6. Also, as mentioned earlier in Chapter 1, this geometry setup breaks the symmetry along the y -axis, leaving us with just one symmetry, along the z -axis.

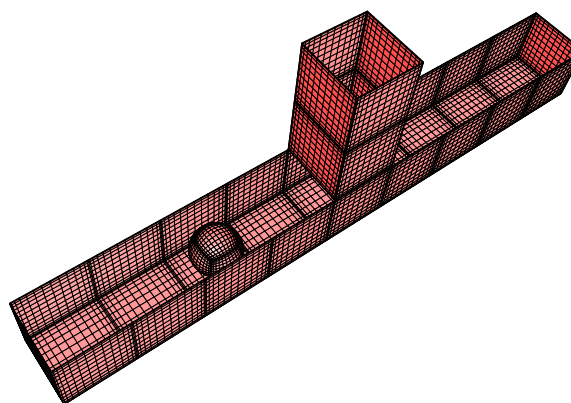
3.2.1 T-junctions with 90° bends (bend radius $r_b = 0$)

A T-junction, with $r_b = 0$ as illustrated in figures 3.16a, 3.15b is used in our study. To allow for comparisons between different geometries, we maintain the same set of parameters for the computations. Figure 3.16 gives the drop displacement along the x , and y -axis respectively. Note that in the case of the cross-junction the drop displacement along the y -axis was zero, because of the symmetric forces along the y -axis. We observe from figure 3.16 that the drop is displaced along the y only in the junction region, and tries to regain axis-symmetry once it crosses the junction.

Figure 3.2.1, gives the droplet velocities along x , y -axis, and also the drop displacement along the y -axis. Note that unlike the case for a cross-junction, we have significant non-zero droplet velocities along the y -direction, which drives a significant displacement along the y -axis. This conveys the fact that the flow in

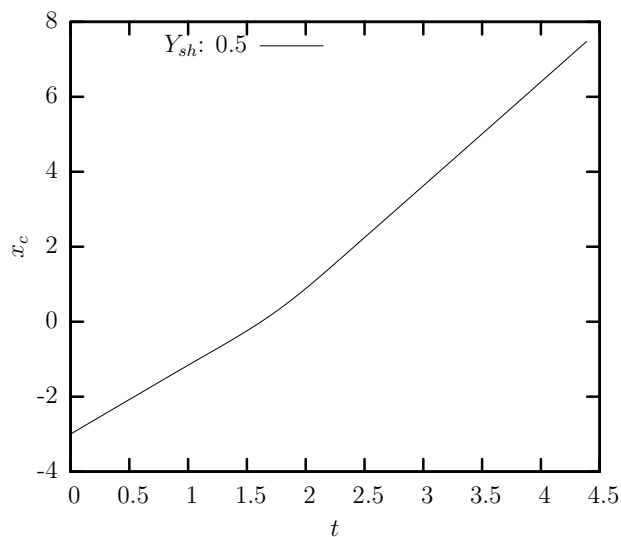


(a) XY-view (with front elements removed)

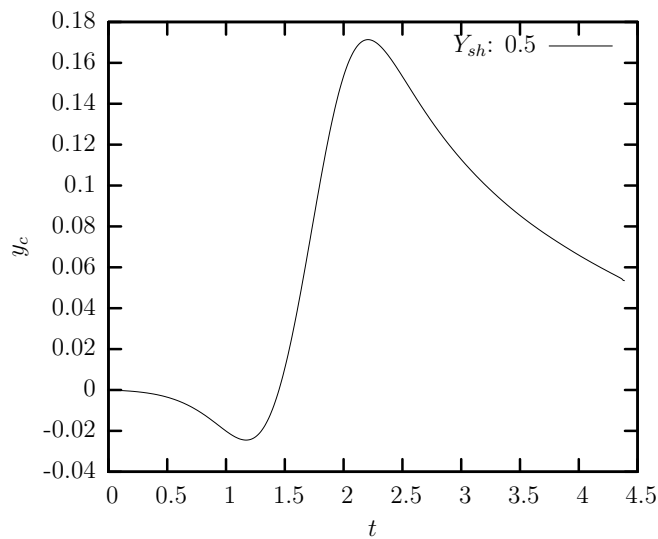


(b) XZ-view (with top elements removed)

Figure 3.15: Illustration of geometry for a T-junction with bend radius $r_b = 0$.



(a) Drop displacement along x -axis



(b) Drop displacement along y -axis

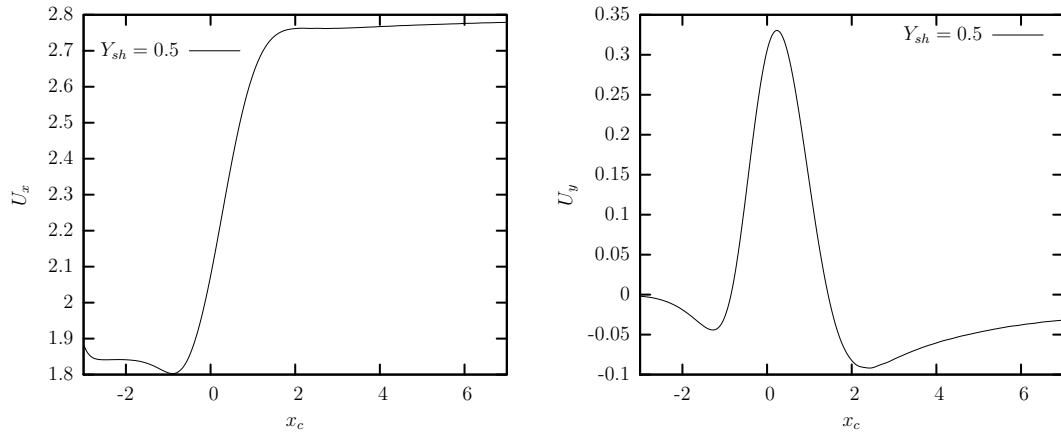
Figure 3.16: Drop displacement along x, y -axes as a function of time t , in a microfluidic T-junction, with bend radius $r_b = 0$, square cross-sectional length $b = 2$, shear rate along x -axis $X_{sh} = 1.0$, shear rate $Y_{sh} = 0.5$ along y -axis, capillary number $Ca = 0.1$ and viscosity ratio $\lambda = 0.2$.

T-junction is not symmetric along the y -axis.

Figure 3.2.1(c) shows that, by the time the drop reaches $x_c = +1$, the drop displaces more than 50% of the initial gap, along the $-y$ -axis. But, once the drop passes the junction region ($x = -1$ to $x = +1$), the drop strives to gain axis symmetry again, as seen from figures 3.2.1(b), and 3.2.1(c). It is interesting to note that, unlike the cross-junction it takes a long time to attain steady-state past the junction.

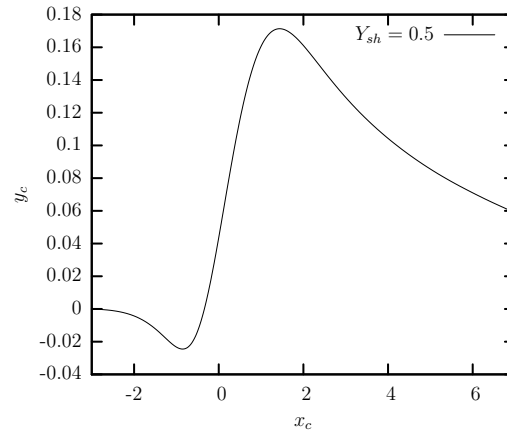
Figure 3.18(a) gives the maximum drop length along the x , y , z -axis respectively, and the drop surface area is given by figure 3.18(b). The excess pressure drop, with respect to single phase flow is plotted in figure 3.18(c). It should be noted that the excess pressure drop for the T-Junction is plotted only considering the inlet and outlet along the x -axis, ignoring the force on the end plate along the y -axis. All these figures corroborate the fact that steady-state is not reached post junction for the T-junction, within the length of our computations geometry.

Figure 3.21 gives the drop shape evolution in a rectangular microfluidic T-junction, with square cross-sections of size 2. The general trends observed are also true for T-junctions with non-zero bend radius. These figures correspond to the case of $Y_{sh} = 0.5$ and $X_{sh} = 1.0$. The key difference in the shape evolution for a T-junction compared to that of a cross-junction is lack of symmetry, and this is evident in the figures here. For example the XY views of the drop in figures 3.21(f), 3.21n, 3.2.1(i) show the drop deformation changing from being peaked at its tip, to its tail. Once the drop crosses the junction, it tries to regain symmetry, but, at the same time is coping with extreme non-symmetric forces, in the junction,



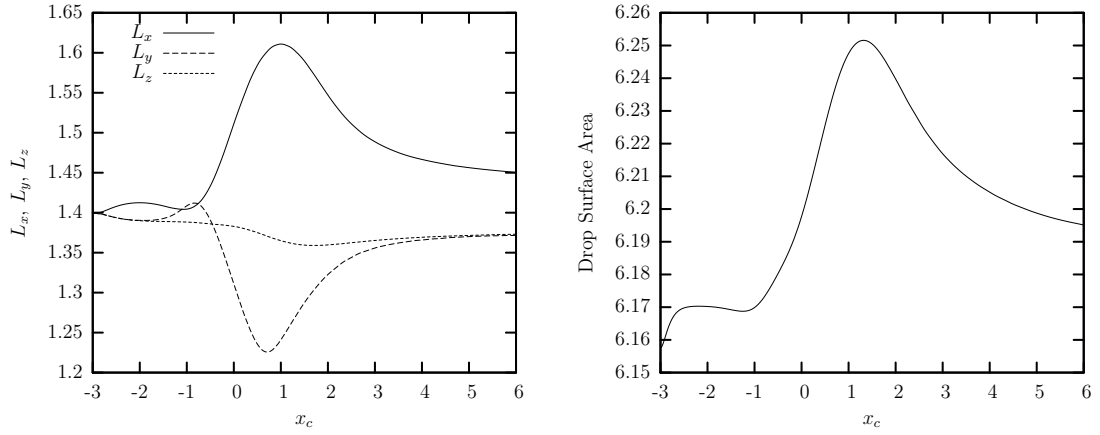
(a) Drop velocity along x -axis, U_x

(b) Drop velocity along y -axis, U_y



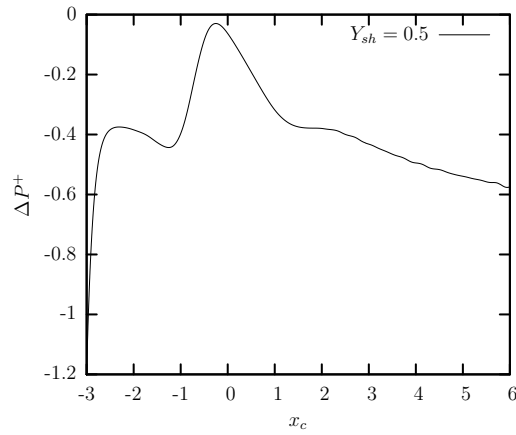
(c) Lateral drop displacement (along y -axis)

Figure 3.17: (a) Drop velocity along x -axis U_x (b) Drop velocity along y -axis U_y (c) Lateral drop displacement with respect to drop position x_c , in a microfluidic T-junction with bend radius $r_b = 0$, square cross-section of length $b = 2$, shear rate along x -axis $X_{sh} = 1.0$, shear rate along y -axis $Y_{sh} = 0.5$ capillary number $Ca = 0.1$ and viscosity ratio $\lambda = 0.2$.



(a) Drop length along x , y , z -axes

(b) Drop surface area



(c) Excess pressure drop along x -axis

Figure 3.18: (a) Maximum droplet length, along x , y and z -axes, (b) Droplet surface area as a function of drop centroid x_c , and (c) Excess pressure drop as a function of drop centroid x_c , in a microfluidic T-junction, with bend radius $r_b = 0$, square cross-section of length $b = 2$, shear rate along x -axis $X_{sh} = 1.0$, varying shear rate along y -axis $Y_{sh} = 0, 0.001, 0.1, 0.5$, capillary number $Ca = 0.1$ and viscosity ratio $\lambda = 0.2$.

which almost cause it to tumble. If the flow is strong enough, the drop would have completely tumbled in the process of crossing the junction, while milder flows would have caused a less dramatic translation, with minor non-symmetric deformations.

Figures 3.19, 3.20 compare the effect of junction smoothness on the drop dynamics. The first thing we observe is that, junction smoothness has a greater effect in the T-junction compared to the cross-junction, this is particularly visible from figure 3.19(c), where the drop displacement along y -axis is large enough to bring the drop very close to the junction walls.

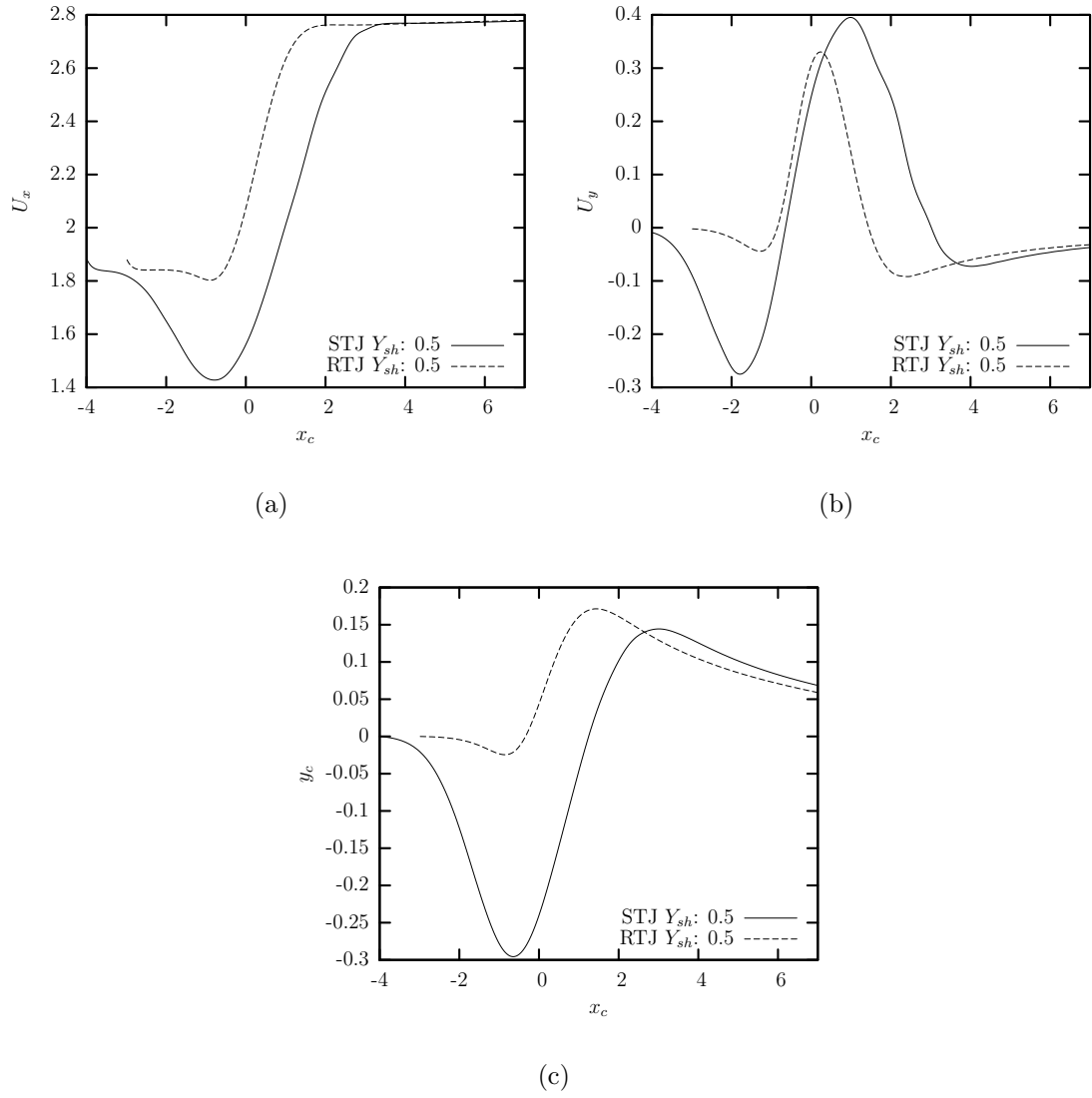


Figure 3.19: (a) Drop velocity U_x along x -axis, (b) Drop velocity U_y along y -axis, (c) Lateral drop displacement (along y -axis) as a function of drop centroid x_c , in microfluidic T-junction, with bend radius $r_b = 0$, and $r_b = 2$, square cross-sectional length $b = 2$, shear rate along x -axis $X_{sh} = 1.0$, shear rate along y -axis $Y_{sh} = 0.5$, capillary number $Ca = 0.1$ and viscosity ratio $\lambda = 0.2$.

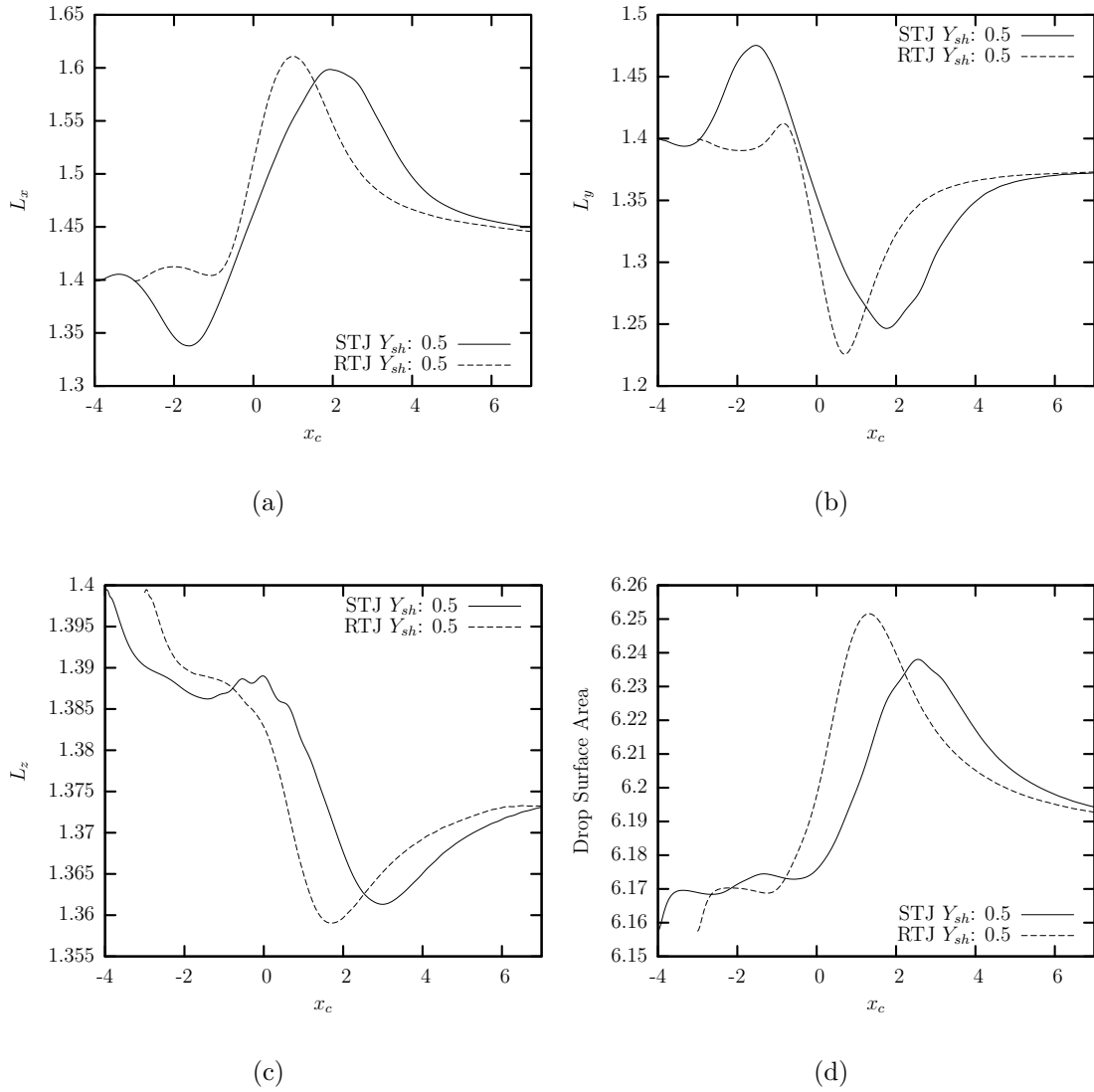
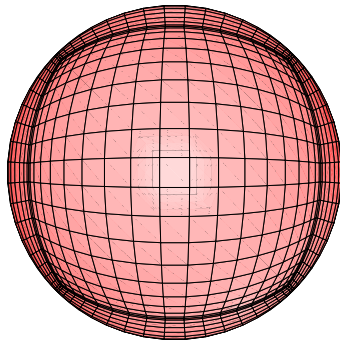
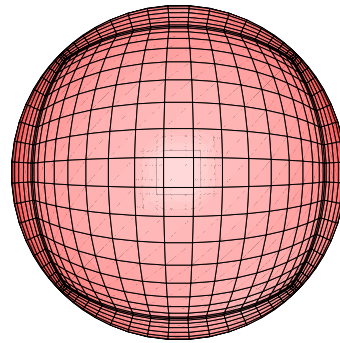


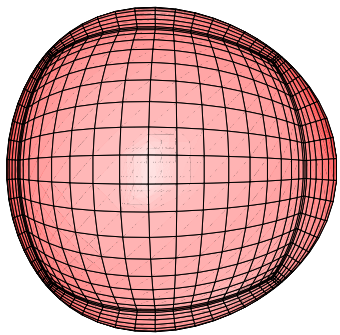
Figure 3.20: Drop length L_x , L_y , L_z along x , y , z -axes respectively and drop surface area as a function of drop centroid x_c in a microfluidic T-junction, with bend radius $r_b = 0$, and $r_b = 2$, square cross-sectional length $b = 2$, shear rate along x -axis $X_{sh} = 1.0$, shear rate along y -axis $Y_{sh} = 0.5$, capillary number $Ca = 0.1$ and viscosity ratio $\lambda = 0.2$.



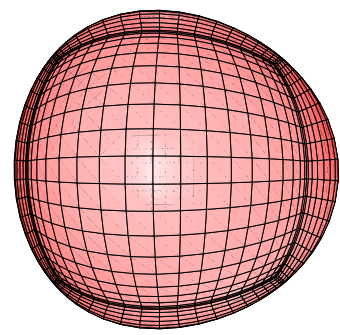
(a) XZ-view: $t = 0$



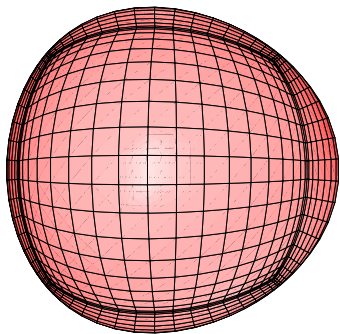
(b) XY-view: $t = 0$



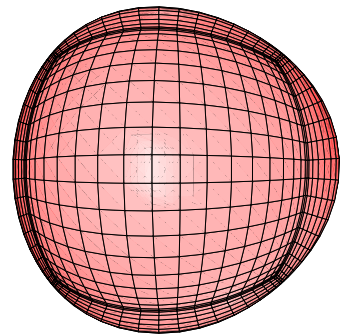
(c) XZ-view: $x_c = -1.727$



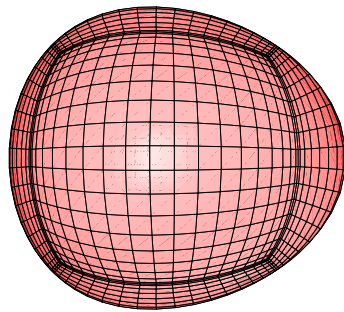
(d) XY-view: $x_c = -1.727$



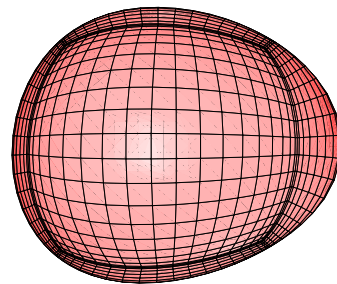
(e) XZ-view: $x_c = -1.016$



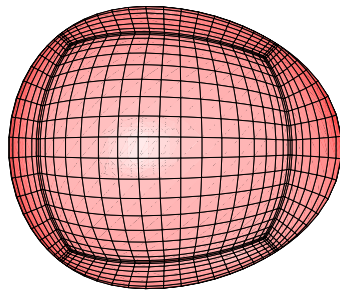
(f) XY-view: $x_c = -1.016$



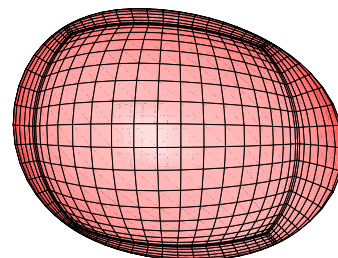
(g) XZ-view: $x_c = 0.124$



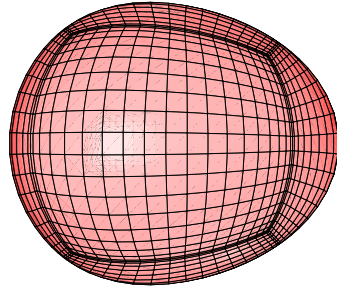
(h) XY-view: $x_c = 0.124$



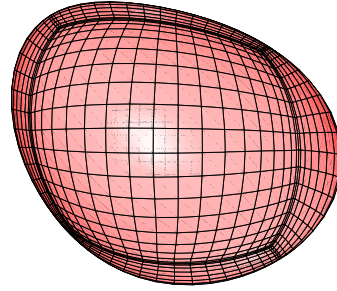
(i) XZ-view: $x_c = 0.833$



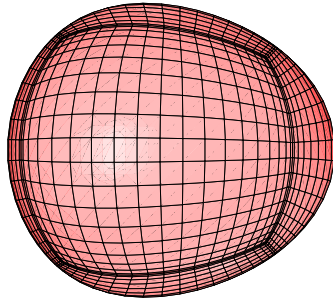
(j) XY-view: $x_c = 0.833$



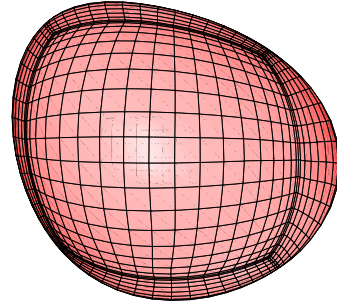
(k) XZ-view: $x_c = 2.052$



(l) XY-view: $x_c = 2.052$



(m) XZ-view: $x_c = 3.211$



(n) XY-view: $x_c = 3.211$

Figure 3.21: Shape evolution of droplet in a microfluidic T-junction, with bend radius $r_b = 0$, square cross-section of length $b = 2$, shear rate along x -axis $X_{sh} = 1.0$, shear rate along y -axis $Y_{sh} = 0.5$, capillary number $Ca = 0.1$ and viscosity ratio $\lambda = 0.2$.

3.3 Conclusions

We have utilized a three-dimensional Spectral Boundary Element algorithm [61] to perform computational studies and determine the drop dynamics in microfluidic T-junctions and cross-junctions, with intersecting lateral flows, for the moderate capillary number of $Ca = 0.1$, varying lateral shear rate Y_{sh} , in the channels along the y -axis, and for two viscosity ratios ($\lambda = 0.2, 20.0$) between the drop and surrounding fluid.

The presence of intersecting flows, in these lateral junctions is found to drastically affect the transient behavior of the drops over the span of the junctions. For the cross-junction geometries, the drop was found to reach equilibrium, almost immediately after crossing the junctions, and also just before entering the junctions. However, for the T-junction geometry, the lack of symmetry of flow in the lateral y -direction, prevents such quick attainment of steady state upon exiting the junction.

Drop velocity was found to be a linear function of the effective shear rate in the corresponding channel, with a sharp gradient in the junction region, whereas parabolic fluctuations were observed in the drop length scales and surface areas. While the individual length scale fluctuations, along the x, y, z -axes were as high as 30% in the junction region, they often acted in a complementary manner, thereby causing the peak drop surface area to fluctuate by around 2%, for the conditions and physical parameters used in our study.

Excess pressure drop at a given spatial coordinate in the junction, defined with

respect to the flow of a single phase fluid in the given geometry, was found to be a strong function of the droplet length, and the peak surface area of the drop in the junction was found to be a non-linear function of the flow rates in the lateral channels, and almost all the surface area increase occurred at the head of the drop, in the direction of the flow. Velocity was found to be a weak, inverse function of the viscosity ratio, the increase in the drop surface areas was found to be greater in drops with lower viscosity. The junction smoothness (bend radius) was found to have a more significant effect on the drop dynamics in a T-junction compared to that in the cross-junction.

Bibliography

- [1] ALEXEEV, A., VERBERG, R., AND BALAZS, A. Patterned surfaces segregate compliant microcapsules. *Langmuir* 23 (2007), 983–987.
- [2] BARTHES-BIESEL, D., AND ACRIVOS, A. Deformation and burst of a liquid droplet freely suspended in a linear shear field. *Journal of Fluid Mechanics* 61, 1 (1973), 1–21.
- [3] BEEBE, D. M. G., AND WALKER, G. Physics and applications of microfluidics in biology. *Ann.Rev.Biomed.Eng* 4 (2002), 261–286.
- [4] BUCKMASTER, J., AND FLAHERTY, J. The bursting of two-dimensional drops in slow viscous flow. *Journal of Fluid Mechanics* 60, 4 (1973), 625–639.
- [5] CHAMBERS, R., AND KOPAC, M. J. The coalescence of living cells with oil drops. i. arbacia eggs immersed in sea water. *Journal of Cellular and Comparative Physiology* 9, 3 (1937), 331–343.
- [6] CHAMPION, J., KATARE, Y., AND MITRAGOTRI, S. Particle shape: a new design parameter for micro-and nanoscale drug delivery carriers. *Journal of controlled release* 16, 121 (2007), 3–9.
- [7] CHAMPION, J., AND MITRAGOTRI, S. Shape induced inhibition of phagocytosis of polymer particles. *Pharmaceutical research* 26, 1 (2009), 244–249.
- [8] CHOW, A. Lab-on-a-chip: opportunities for chemical engineering. *AIChE Journal* 48, 8 (2002), 1590–1595.
- [9] CHRISTOPHER, G., AND ANNA, S. Passive breakup of viscoelastic droplets and filament self-thinning at a microfluidic t-junction. *Journal of Rheology* 53, 3 (2009), 663–683.
- [10] CHRISTOPHER, G., BERGSTEIN, J., END, N., AND POON, M. Coalescence and splitting of confined droplets at microfluidic junctions. *Lab on a Chip* 9 (2009), 1102–1109.
- [11] CHUNG, C., HULSEN, M., KIM, J., AND AHN, K. Numerical study on the effect of viscoelasticity on drop deformation in simple shear and 5:1:5 planar contraction/expansion microchannel. *J Non-Newton Fluid* 155 (2008), 80–93.
- [12] CHUNG, C., KIM, J. M., AHN, K. H., AND LEE, S. J. Numerical study on the effect of viscoelasticity on pressure drop and film thickness for a droplet flow in a confined microchannel. *Korea-Australia Rheology Journal* 21, 1 (2009), 59–69.
- [13] COLLINS, J., AND LEE, A. Control of serial microfluidic droplet size gradient by step-wise ramping of flow rates. *Microfluid Nanofluid* 3 (2007), 19–25.

- [14] CUBAUD, T. Deformation and breakup of high-viscosity droplets with symmetric microfluidic cross flows. *Physical Review E* 80, 026307 (2009), 1–4.
- [15] CUBAUD, T., AND HO, C. Transport of bubbles in square microchannels. *Physics of Fluids* 16, 12 (2004), 4575–4585.
- [16] CUBAUD, T., AND MASON, T. Capillary threads and viscous droplets in square microchannels. *Physics of Fluids* 20, 053302 (2008), 1–11.
- [17] DENDUKURI, D., TSOI, K., HATTON, T., AND DOYLE, P. Controlled synthesis of nonspherical microparticles using microfluidics. *Langmuir* 21 (2005), 2113–2116.
- [18] DER GRAAF, S. V., STEEGMANS, M., VAN DER SMAN, R., SCHROEN, C., AND R.M.Boom. Droplet formation in a t-shaped microchannel junction: a model system for membrane emulsification. *Colloids and Surfaces A: Physicochem. Eng. Aspects* 266 (2005), 106–116.
- [19] DIMITRAKOPOULOS, P. Deformation of a droplet adhering to a solid surface in shear flow: onset of interfacial sliding. *Journal of Fluid Mechanics* 580 (2007), 451–466.
- [20] DIMITRAKOPOULOS, P. Gravitational effects on the deformation of a droplet adhering to a horizontal solid surface in shear flow. *Physics of Fluids* 19, 12 (2007), 122105.
- [21] DIMITRAKOPOULOS, P. Interfacial dynamics in stokes flow via a three-dimensional fully-implicit interfacial spectral boundary element algorithm. *Journal of Computational Physics* 225 (2007), 408–426.
- [22] DIMITRAKOPOULOS, P., AND HIGDON, J. Displacement of fluid droplets from solid surfaces in low-reynolds-number shear flows. *Journal of Fluid Mechanics* 336 (1997), 351–378.
- [23] DIMITRAKOPOULOS, P., AND HIGDON, J. On the displacement of three-dimensional fluid droplets from solid surfaces in low-reynolds-number shear flows. *Journal of Fluid Mechanics* 377 (1998), 189–222.
- [24] DIMITRAKOPOULOS, P., AND HIGDON, J. On the gravitational displacement of three-dimensional fluid droplets from inclined solid surfaces. *Journal of Fluid Mechanics* 395 (1999), 181–209.
- [25] DIMITRAKOPOULOS, P., AND HIGDON, J. On the displacement of three-dimensional fluid droplets adhering to a plane wall in viscous pressure-driven flows. *Journal of Fluid Mechanics* 435, 327–350 (2001).
- [26] DIMITRAKOPOULOS, P., AND HIGDON, J. On the displacement of fluid bridges from solid surfaces in viscous pressure-driven flows. *Physics of Fluids* 15, 10 (2003), 3255–3258.

- [27] DOERR, A. Mass spectrometers on a chip. *Nature Methods* 6, 8 (2009), 555.
- [28] EVANKO, D. Living droplets. *Nat Meth* 5, 7 (2008), 580–581.
- [29] FUERSTMAN, M., LAI, A., THURLOW, M., AND SHEVKOPLYAS, S. The pressure drop along rectangular microchannels containing bubbles. *Lab on a Chip* 7 (2007), 1479–1489.
- [30] GARSTECKI, P., FUERSTMAN, M., STONE, H., AND WHITESIDES, G. Formation of droplets and bubbles in a microfluidic t-junction—scaling and mechanism of break-up. *Lab on a Chip* 6 (2006), 437–446.
- [31] JANASEK, D., FRANZKE, J., AND MANZ, A. Scaling and the design of miniaturized chemical-analysis systems. *Nature* 442 (2006), 374–380.
- [32] JOHNSON, R., AND SADHAL, S. Fluid mechanics of compound multiphase drops and bubbles. *Annu Rev Fluid Mech* 17 (1985), 289–320.
- [33] JULLIEN, M., CHING, M., COHEN, C., AND MENETRIER, L. Droplet breakup in microfluidic t-junctions at small capillary numbers. *Physics of Fluids* 21, 072001 (2009), 1–6.
- [34] LESHANSKY, A., AND PISMEN, L. Breakup of drops in a microfluidic t-junction. *Physics of Fluids* 21, 023303 (2009), 1–6.
- [35] LI, J., BULUSU, V., AND GUPTA, N. Buoyancy-driven motion of bubbles in square channels. *Chemical Engineering Science* 63 (2008), 3766–3774.
- [36] MENECH, M. D., GARSTECKI, P., JOUSSE, F., AND STONE, H. Transition from squeezing to dripping in a microfluidic t-shaped junction. *Journal of Fluid Mechanics* 595 (2008), 141–161.
- [37] MICHAELIDES, E. *Particles, bubbles & drops: their motion, heat and mass transfer*. Word Scientific Publishing, 2006.
- [38] MITRAGOTRI, S. In drug delivery, shape does matter. *Pharmaceutical research* 26, 1 (2009), 232–234.
- [39] NAVOT, Y. Critical behavior of drop breakup in axisymmetric viscous flow. *Physics of Fluids* 11, 5 (1999), 990–996.
- [40] NISISAKO, T., AND TORII, T. Microfluidic large-scale integration on a chip for mass production of monodisperse droplets and particles. *Lab on a Chip* 8 (2008), 287–293.
- [41] POZRIKIDIS, C. *Boundary Integral and Singularity Methods for Linearized Viscous Flow*. Cambridge University Press, Cambridge, 1999.

- [42] PREGIBON, D., TONER, M., AND DOYLE, P. Multifunctional encoded particles for high-throughput biomolecule analysis. *Science* 315, 5817 (2007), 1393–1396.
- [43] QU, W., MUDAWAR, I., LEE, S., AND WERELEY, S. Experimental and computational investigation of flow development and pressure drop in a rectangular micro-channel. *Journal of Electronic Packaging* 128 (2006), 1–9.
- [44] RALLISON, J. A numerical study of the deformation and burst of a viscous drop in general shear flows. *Journal of Fluid Mechanics* 109 (1981), 465–482.
- [45] RALLISON, J. The deformation of small viscous drops and bubbles in shear flows. *Annu Rev Fluid Mech* 16 (1984), 45–66.
- [46] RALLISON, J., AND ACRIVOS, A. A numerical study of the deformation and burst of a viscous drop in an extensional flow. *Journal of Fluid Mechanics* 89, 1 (1978), 191–200.
- [47] SCHUCHMAN, E., MITRAGOTRI, S., AND MUZYKANTOV, V. Control of endothelial targeting and intracellular delivery of therapeutic enzymes by modulating the size and shape of icam-1-targeted carrier. *Molecular Therapy* 16, 8 (2008), 1450–1458.
- [48] SHIRANI, E., AND MASOOMI, S. Deformation of a droplet in a channel flow. *J Fuel Cell Sci Tech* 5, 041008 (2008), 1–8.
- [49] SQUIRES, T., AND QUAKE, S. Microfluidics: Fluid physics at the nanoliter scale. *Reviews of modern physics* 77 (2005), 977–1026.
- [50] STONE, H., STROOCK, A., AND AJDARI, A. Engineering flows in small devices: Microfluidics toward a lab-on-a-chip. *Annual Rev Fluid Mech* 36 (2004), 381–411.
- [51] TAKEMURA, F., MAGNAUDET, J., AND DIMITRAKOPOULOS, P. Migration and deformation of bubbles rising in a wall-bounded shear flow at finite reynolds number. *Journal of Fluid Mechanics* 634 (2009), 463–486.
- [52] TAN, J., XU, J., LI, S., AND LUO, G. Drop dispenser in a cross-junction microfluidic device: Scaling and mechanism of breakup. *Chemical Engineering Journal* 136 (2008), 306–311.
- [53] TAN, Y., CRISTINI, V., AND LEE, A. Monodispersed microfluidic droplet generation by shear focusing microfluidic device. *Sensors & Actuators: B. Chemical* 114 (2006), 350–356.
- [54] TAYLOR, G. The viscosity of a fluid containing small drops of another fluid. *Proceedings of the Royal Society of London. Series A* 138, 834 (1932), 41–48.

- [55] TAYLOR, G. The formation of emulsions in definable fields of flow. *Proceedings of the Royal Society of London. Series A* 146, 858 (1934), 501–523.
- [56] TAYLOR, G. Conical free surfaces and fluid interfaces. *Proceedings of the 11th International Congress in Applied Mechanics* (1964).
- [57] VANAPALLI, S. A., BANPURKAR, A. G., VAN DEN ENDE, D., DUIJS, M. H. G., AND MUGELE, F. Hydrodynamic resistance of single confined moving drops in rectangular microchannels. *Lab on a Chip* 9, 7 (2009), 982–990.
- [58] WANG, Y. *Flow and Interfacial Dynamics in Vascular Vessels and Microfluidics*. PhD thesis, University of Maryland, College Park.
- [59] WANG, Y., AND DIMITRAKOPOULOS, P. Nature of the hemodynamic forces exerted on vascular endothelial cells or leukocytes adhering to the surface of blood vessels. *Physics of Fluids* 18, 087107 (2006), 1–14.
- [60] WANG, Y., AND DIMITRAKOPOULOS, P. Normal force exerted on vascular endothelial cells. *Physical Review Letters* 96, 028106 (2006), 1–4.
- [61] WANG, Y., AND DIMITRAKOPOULOS, P. A three-dimensional spectral boundary element algorithm for interfacial dynamics in stokes flow. *Physics of Fluids* 18, 082106 (2006), 1–16.
- [62] WANG, Y., DODSON, W., AND DIMITRAKOPOULOS, P. Dynamics of multiphase flows via spectral boundary elements and parallel computations. *Parallel Computational Fluid Dynamics: Theory and Applications* (2006), 405–412.
- [63] WARRICK, J., MEYVANTSSON, I., JU, J., AND BEEBE, D. High-throughput microfluidics: improved sample treatment and washing over standard wells. *Lab on a Chip*.
- [64] WHITESIDES, G. The origins and the future of microfluidics. *Nature* 442 (2006), 368–373.
- [65] WU, L., TSUTAHARA, M., KIM, L. S., AND HA, M. Three-dimensional lattice boltzmann simulations of droplet formation in a cross-junction microchannel. *Int J Multiphas Flow* 34, 9 (2008), 852–864.
- [66] YEH, C. H., AND LIN, Y. C. Using a cross-flow microfluidic chip for monodisperse uv-photopolymerized microparticles. *Microfluid Nanofluid* 6, 2 (2009), 277–283.
- [67] YIH, C.-S. *Fluid Mechanics*. West River Press, 1988.
- [68] YOUNGREN, G., AND ACRIVOS, A. Stokes flow past a particle of arbitrary shape: a numerical method of solution. *Journal of Fluid Mechanics* 69, 2 (1975), 377–403.

- [69] YOUNGREN, G., AND ACRIVOS, A. On the shape of a gas bubble in a viscous extensional flow. *Journal of Fluid Mechanics* 76, 3 (1976), 433–442.
- [70] ZHU, G., ALEXEEV, A., AND BALAZS, A. Designing constricted microchannels to selectively entrap soft particles. *Macromolecules* 40 (2007), 5176–5181.

Vita

Sai Kishore Mamidi was born in July 1986, in Hyderabad, India. After completion of his high school from St.Patrick's, with honors in May 2003, he enrolled in the Chemical Engineering program at Manipal University, Karnataka, India, where he was the valedictorian of his graduating batch in May 2007. His undergraduate thesis focused on the inverse modeling problem, with the title "Parameter Estimation in Chemical Systems Exhibiting Complex Dynamics". In September 2007, he was enrolled at the graduate program of the Department of Chemical and Biomolecular Engineering at the University of Maryland at College Park. He conducted research in the area of computational fluid dynamics under the guidance of Professor Panagiotis Dimitrakopoulos. His graduate work involved the study of interfacial drop dynamics in microfluidic cross-junctions and T-Junctions. In January 2010, he defended his thesis, titled "Computational Studies on Droplet Dynamics at Intersecting Flows in Microfluidic Junctions". for the degree of Master of Science in Chemical Engineering.